Electrochimica Acta 540 (2025) 147226

Contents lists available at ScienceDirect

Electrochimica Acta

journal homepage: www.journals.elsevier.com/electrochimica-acta

Low-cost transition metals (Fe, Ni, Co) on carbon aerogel for water electrolysis and supercapacitor applications

Dušan Mladenović [a,†], Marta Martins [b,†], Meryem Samancı [c], Miguel Charneca [b], Anup Paul [d], Diogo M.F. Santos [b], Ayşe Bayrakçeken [c,e], Biljana Šljukić [a,b,*]

[a] University of Belgrade, Faculty of Physical Chemistry, Studentski trg 12-16, 11158 Belgrade, Serbia
[b] Center of Physics and Engineering of Advanced Materials, Laboratory of Physics for Materials and Emerging Technologies, Chemical Engineering Department, Instituto Superior Técnico, Universidade de Lisboa, 1049-001 Lisbon, Portugal
[c] Department of Chemical Engineering, Atatürk University, Erzurum, 25240, Turkey
[d] Centro de Estudos de Engenharia Química, Instituto Superior de Engenharia de Lisboa, Instituto Politécnico de Lisboa, Lisboa, Portugal
[e] Department of Nanoscience and Nanoengineering, Atatürk University, Erzurum 25240, Turkey

ARTICLE INFO

Keywords:
Transition metal
Carbon aerogel
Nitrogen-doped catalyst
Water electrolysis
Supercapacitors

ABSTRACT

Cost-effective transition metals (TM = Fe, Ni, Co) were immobilized on carbon aerogel (CA) using microwave irradiation, followed by nitrogen doping into one catalyst series through heat treatment. The physical characterization of the synthesized catalysts included N_2 sorption, inductively coupled plasma-mass spectrometry, X-ray diffraction analysis, transmission electron microscopy, Raman spectroscopy, FTIR spectroscopy, and X-ray photoelectron spectroscopy. Co/CA displayed the best performance for oxygen evolution reaction (OER) electrocatalysis in alkaline water electrolysis, followed by Ni/CA. Co/CA exhibited a small Tafel slope of 110 mV dec^{-1} and required an overpotential of just 276 mV to reach 10 mA cm^{-2}, lower than that of the commercial IrO_2 electrocatalyst. Additionally, Co/CA and Ni/CA demonstrated excellent long-term stability during OER, with activity increasing over time. Capacitance measurements also showed the potential of TM/CA materials as supercapacitor electrodes. Fe/CA achieved the highest performance, with a specific capacitance of 322 F g^{-1} at a moderate current of 1 A g^{-1}. It retained up to 96 % of its capacitance over 1000 cycles, indicating excellent stability.

1. Introduction

The increasing global population and rapid advancements in technology have led to a rise in energy consumption and a rapid depletion of fossil fuel reserves. This has further triggered a surge in carbon dioxide emission rates, accompanied by increased environmental pollution and global warming. This situation has led humanity to develop renewable energy sources and sustainable technologies (green energy systems). Promising progress has been made in green energy systems, where energy is converted (e.g., using fuel cells with green hydrogen produced in water electrolyzers) and stored (e.g., in supercapacitors and batteries). A series of electrochemical reactions takes place in these systems; however, these reactions are generally catalyzed by catalysts based on platinum-group metals, which are both expensive and rare. This limits the industrial applications of energy systems. To overcome these limitations, transition metal (TM)-based electrocatalysts have garnered significant attention in recent years owing to their abundant resources, low cost, and catalytic performance comparable to that of noble metals [1].

Considering the abundance and accessibility of water resources worldwide, water electrolyzers, which can "convert" the generated electricity into storable hydrogen, are an exciting technology. Water splitting systems have critical issues, such as the slow kinetics of the oxygen evolution reaction (OER), which involves the transfer of four electrons at the anode (Eq. (1)).

$$4OH^- \rightarrow O_2 + 2H_2O + 4e^- \quad (1)$$

Over the last 15 years, significant efforts have been made to develop

* Corresponding author at: Center of Physics and Engineering of Advanced Materials, Laboratory of Physics for Materials and Emerging Technologies, Chemical Engineering Department, Instituto Superior Técnico, Universidade de Lisboa, 1049-001 Lisbon, Portugal.
E-mail address: biljana.paunkovic@tecnico.ulisboa.pt (B. Šljukić).
† Equally contributed.

https://doi.org/10.1016/j.electacta.2025.147226
Received 18 July 2025; Received in revised form 20 August 2025; Accepted 22 August 2025
Available online 22 August 2025

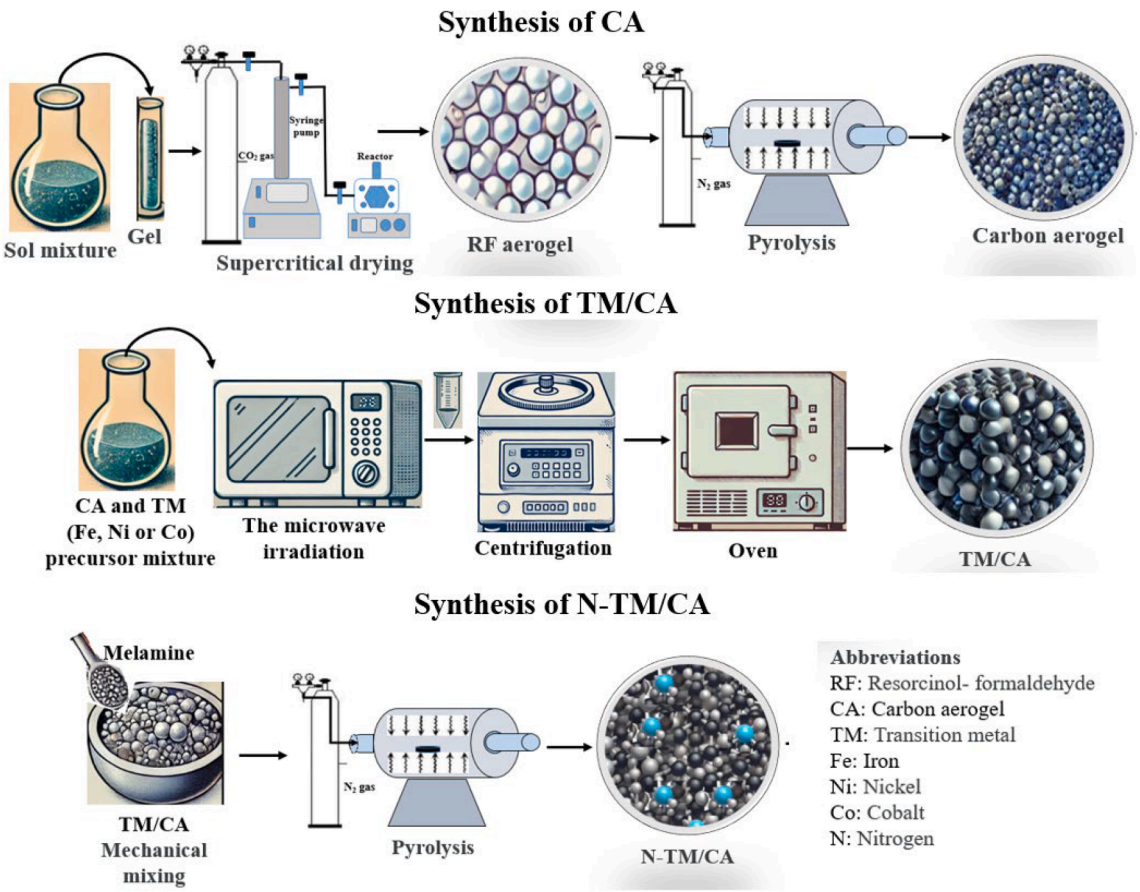

Fig. 1. Schematic representation of the three-step catalysts' synthesis procedure.

OER electrocatalysts based on transition metal elements (especially Fe, Ni, and Co) with low cost, high efficiency, and excellent stability [2]. In parallel, it has been elucidated that the electronic properties of carbon materials can be adjusted by doping their structures with heteroatoms such as N, B, and S. Transition metals, as well as heteroatom-doped carbon catalysts, have been reported to exhibit notable catalytic activities, further motivating the development of composite materials approaches [3].

It is well-documented that catalyst support materials have a significant impact on the performance of the catalyst in electrochemical processes. Therefore, a catalyst support material must have a high specific surface area to ensure high and stable dispersion of metals. The support material must interact strongly with metal particles and have high electrical conductivity to facilitate electron transfer. As a result, appropriately selected support material for any process can significantly increase the electrocatalytic activity [4]. Aerogels have recently garnered attention for their use in electrochemical energy conversion and storage, owing to their large surface area, high porosity, and good electrical conductivity [5]. The unique properties of these structures, which include abundant catalytically active sites, fast electron transfer, and excellent structural stability, are all beneficial for electrocatalysis [6]. Thus, 3D aerogel skeletons have been used as catalyst supports or electrocatalysts in recent years. For instance, (Ni,Co)Se_2GA (with GA being graphene aerogel) exhibited high activity for the OER, requiring a low overpotential of 250 mV to achieve a current density of 10 mA cm^{-2} under alkaline conditions [7]. This example illustrates well the trend of coupling low-cost TMs and aerogels for electrocatalysis applications. Recent studies on non-noble TM (Ni, Mo, Co, Fe, W)-based catalysts and their compounds (carbides, phosphides, nitrides, and sulfides) demonstrated not only their excellent activity, but also chemical stability and sufficient corrosion resistance in alkaline media, reinforcing their potential for OER [8–10].

Carbon aerogels (CAs) are recognized as promising materials for electrodes in supercapacitors, delivering high power density at fast charge/discharge rates, along with long cycle life and low cost [11,12]. For example, activated CAs demonstrated a specific capacitance, C_s, of up to 89.1 F g^{-1}, with a high capacitance retention of 93.2 % after 3000 cycles [13]. Another CA using sugarcane juice as a carbon source was tested for 5500 cycles, showing 70 % capacitance retention at 30 mA cm^{-2} [14]. 3D-printed CAs also exhibited high energy storage capacitance [15].

As mentioned, one way to further enhance the aerogel's performance is the incorporation of heteroatoms such as nitrogen, which can be incorporated into carbon networks by changing the electron distribution and bonding of the carbon surface [16]. Several studies have highlighted the importance of doping with nitrogen and explored the relationship between the composition and properties of nitrogen-doped carbon aerogels (N-CAs). For example, a single Ni metal atom anchored on N-doped carbon aerogel (Ni-SA)@NCA) catalyst exhibited excellent OER activity, with an overpotential of 380 mV at a current density of 10 mA cm^{-2} and a low Tafel slope of 89.8 mV dec^{-1}, indicating an excellent O_2 evolution kinetics [17]. Fe–Ni alloy nanoclusters supported on N, S co-doped carbon aerogel (Fe–Ni ANC@NSCA) also demonstrated high performance for OER in alkaline media with an overpotential of 260 mV at 10 mA cm^{-2} [18].

This study introduces a novel synthesis strategy that integrates complementary techniques to develop high-performance CA-based catalysts for multifunctional electrochemical applications. The approach starts with supercritical drying to generate a high-surface-area CA support. The CA support itself, previously investigated as an effective standalone catalyst for oxygen reduction and energy storage [19,20], provides a strong foundation for further performance enhancement

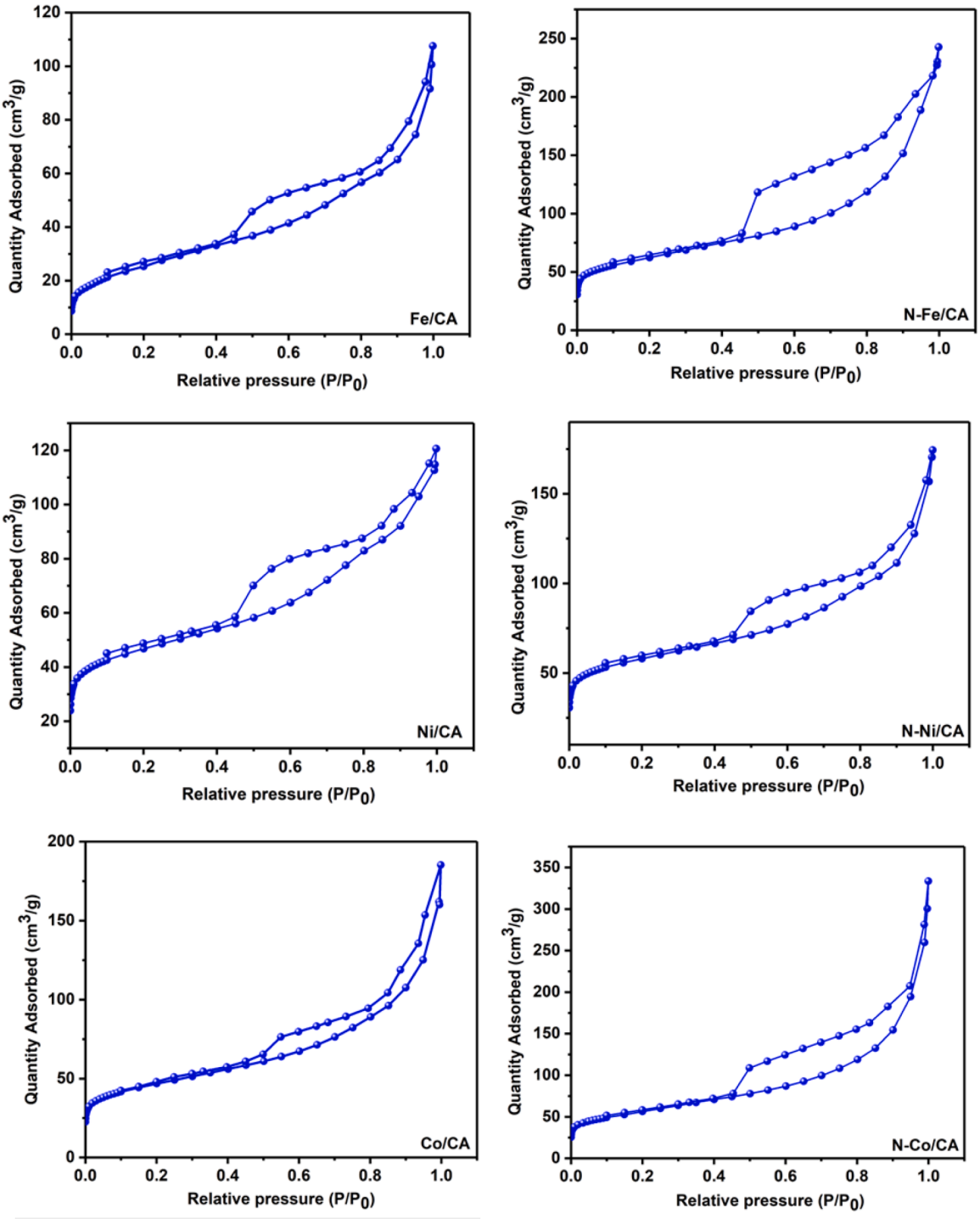

Fig. 2. N_2-sorption isotherms at 77 K for Fe/CA, N-Fe/CA, Ni/CA, N-Ni/CA, Co/CA, and N-Co/CA.

through the incorporation of transition metals. Thus, in the following step, microwave-assisted immobilization of transition metals (Fe, Ni, Co) is achieved with rapid, uniform heating and homogeneous metal dispersion across the CA support. Finally, nitrogen doping is achieved via pyrolysis to further tailor the electronic structure and catalytic activity of the prepared materials. This combination of methods enables efficient interaction between the CA support and the transition metals, leading to enhanced catalytic properties. Importantly, this work advances beyond prior studies that have typically focused on either OER electrocatalysis or supercapacitor performance. Herein, the dual applicability of TM/CA catalysts was systematically evaluated through comprehensive physical (ICP-MS, N_2 sorption, XRD, FTIR, Raman spectroscopy, TEM, and XPS) and electrochemical analyses. The materials' effectiveness was demonstrated, thereby offering a cost-effective alternative to noble-metal-based systems for electrochemical energy conversion and storage.

2. Materials synthesis

Chemicals used in the materials synthesis and throughout the study are listed in the Supplementary Information. Material syntheses were carried out in three stages. In the first stage, CA support material was

synthesized. In the second stage, loading of transition metal (Fe, Ni, Co) on the CA support was done using the microwave irradiation method. In the last stage, doping with N was achieved using the heat treatment method. A schematic representation of these synthesis stages is given in Fig. 1.

Synthesis of carbon aerogel (CA). CA was prepared by the polymerization of resorcinol (R) and formaldehyde (F) in the presence of pure water (W) and a catalyst (C, Na_2CO_3) using the sol-gel method [19]. The sol solution was prepared with molar ratios of $R/C = 200$, $R/W = 0.02$, and $R/F = 0.5$. The sol solution was placed in a closed glass tube and kept at room temperature for 24 h to allow gelation to occur. Then, the glass tube was placed in the oven at 50 °C for 24 h and at 90 °C for 72 h. The gel was removed from the glass tube, placed in a beaker filled with acetone, and kept for 24 h. At this stage, the solvent change process was carried out. The gel was then placed in the supercritical reactor with acetone. The gel was extracted and dried with supercritical carbon dioxide at 2000 psi and 50 °C. After this stage, the R-F aerogel structure was obtained and pyrolyzed in a N_2 environment at 1000 °C for 4 h to reach the final CA structure.

Synthesis of transition metal (Fe, Ni, Co)/CA catalysts. In heterogeneous catalysts, an optimum metal loading should provide a good distribution while maintaining a high density of active sites [21,22]. In our previous heterogeneous catalyst studies, when high-cost precious metals were added to carbonaceous support materials, the metal loading ratio was typically set at 20 wt. %, which was the nominal value [23,24]. In this study, since CA-supported low-cost transition metal catalysts were synthesized, the aim was to provide a balance between high activity and structural stability with metal loadings in the range of 30–50 wt. %. A lower loading (less than 30 wt. %) results in fewer active sites, which leads to a decrease in catalytic efficiency. A higher loading (more than 50 wt. %) negatively affects catalyst performance by causing irregular accumulation of metal nanoparticles (reducing surface area due to agglomeration), local overheating, or sintering [25]. Microwave irradiation supports rapid and uniform metal deposition, and a loading of 40 wt. % is within the range where efficient metal incorporation can be achieved without excessive clustering [26].

The microwave irradiation method was used to synthesize transition metal catalysts supported by CA [27]. Synthesis was based on 100 mg CA, aiming for a 40 wt. % metal loading on the support material. CA and the transition metal precursors ($NiCl_2{\cdot}6H_2O$, $FeCl_3{\cdot}6H_2O$, or Co $(NO_3)_2{\cdot}6H_2O$) were thoroughly dissolved in a glass beaker with 10 mL of pure water in an ultrasonic bath for 30 min. 30 mL of ethylene glycol was then added to this mixture, which was mixed for 30 min in a magnetic mixer. The pH of the mixture was then increased to 13 by adding a 2 M KOH solution and mixing for 2.5 h at room temperature. The mixture was then placed in the microwave oven for 1 min at 800 W power. The mixture removed from the microwave oven was quickly transferred to the ice bath. The cooled mixture was placed in the centrifuge and washed with pure water at 7000 rpm, with a sequence of 15 min, 5 min, and 5 min. The solid mixture that fell to the bottom of the centrifugal tube and separated from the waste parts (liquid and residual metal precursors) was kept at 90 °C for 24 h. Additionally, the catalysts were placed in an oven and pyrolyzed at 500 °C for 2 h in a N_2 atmosphere to eliminate any impurities. The catalysts obtained were named Fe/CA, Ni/CA, and Co/CA.

Synthesis of nitrogen-doped transition metal/CA catalysts. Melamine was used as a source of nitrogen [28]. The melamine and transition metal/CA ratio was set to 1:1. The mixture was mechanically mixed in a ceramic mortar for 30 min to ensure homogeneity. It was then placed in a tubular oven and pyrolyzed in an N_2 atmosphere at 1000 °C for 2 h. The catalysts obtained were named N-Fe/CA, N-Ni/CA, and N-Co/CA.

Experimental details of materials' physicochemical and electrochemical characterization are given in the Supplementary Information.

Table 1
ICP-MS results, average crystal size, and average particle size analyses of the catalysts.

Catalyst	ICP-MS (wt. %)			XRD average crystal size (nm)	TEM average particle size (nm)
	Fe	Ni	Co		
Fe/CA	34.3	–	–	15.7	38.3
N-Fe/CA	44.2	–	–	21.9	51.6
Ni/CA	–	36.6	–	18.4	40.0
N-Ni/CA	–	71.3	–	25.2	51.9
Co/CA	–	–	48.9	17.6	41.8
N-Co/CA	–	–	47.7	20.0	52.0

3. Results and discussion

3.1. Characterization of catalysts

High BET surface area in electrochemical catalysts maximizes the number of active sites available for reactions. Optimized porosity, with tailored pore sizes, ensures efficient transport of reactants to these sites and products away, minimizing diffusion limitations and enhancing catalyst performance [29–31]. Before proceeding to catalyst synthesis, the carbon aerogel (CA), with a specific surface area of 664 $m^2\ g^{-1}$, an average pore size of 9.6 nm, and a generally mesoporous form, was synthesized by the supercritical drying method as a support material with optimum surface properties to make the catalyst more effective [19]. The TM-CAs were synthesized using the microwave method using Fe, Ni, and Co precursors. Then, N-doped TM catalysts were synthesized using melamine as a nitrogen source and applying heat treatment. The corresponding BET surface areas of the synthesized TM-CAs (Fe/CA, N-Fe/CA, Ni/CA, N-Ni/CA, Co/CA, and N-Co/CA) were also determined using N_2-sorption isotherms (Fig. 2). The BET surface area values were: 93 $m^2\ g^{-1}$ for Fe/CA, 215 $m^2\ g^{-1}$ for N-Fe/CA, 158 $m^2\ g^{-1}$ for Ni/CA, 195 $m^2\ g^{-1}$ for N-Ni/CA, 161 $m^2\ g^{-1}$ for Co/CA, and 198 $m^2\ g^{-1}$ for N-Co/CA, respectively, indicating a moderate degree of porosity. All samples exhibited Type IV isotherms typical of microporous materials and H3 hysteresis loops, suggesting the presence of mesopores. Non-linear density functional theory (NLDFT) pore-size distribution analysis (**Figure S1**) revealed a dominant micropore population centered at ca. 1.2 nm in all materials, along with notable mesoporous features.

ICP-MS analysis was performed to determine the amount of metal mass loaded on the support material (Table 1). In nitrogen-free catalysts, the lowest metal loading was 34.3 wt. % for the Fe/CA catalyst, while the highest metal loading of ca. 49 wt. % was achieved for the Co/CA catalyst. In this way, small deviations from the intended loading of 40 wt. % occurred depending on the type of transition metal. While the metal content increased with nitrogen doping in Fe and Ni catalysts, the metal content in Co catalysts remained almost unchanged. The Ni loading of the N-Ni/CA catalyst (71.3 wt. %) is considerably higher than that of the other catalysts. This may be attributed to several reasons. First, the difference in the Tammann temperature of the three metals resulted in variations in metal loading ratios. Tammann temperature is the temperature at which the atoms of a solid acquire sufficient thermal energy for their mass mobility and activity to become appreciable [32]. In other words, above the Tammann temperature, metal particles tend to collide with each other and form agglomerates. The Tammann temperature of Ni metal is lower than that of Fe and Co metals (Fe: 632 °C, Co: 612 °C, Ni: 592 °C) [33]. Second, during the heat treatment step for N doping, Ni particles may have undergone more efficient aggregation or redistribution compared to Fe and Co [34]. This led to a higher measured concentration in the final catalyst. Additionally, Ni has stable interactions with nitrogen-containing functional groups (pyridinic or graphitic N) that enhance retention on CA [35]. The third reason is that ICP-MS analysis measures total metal content but does not distinguish

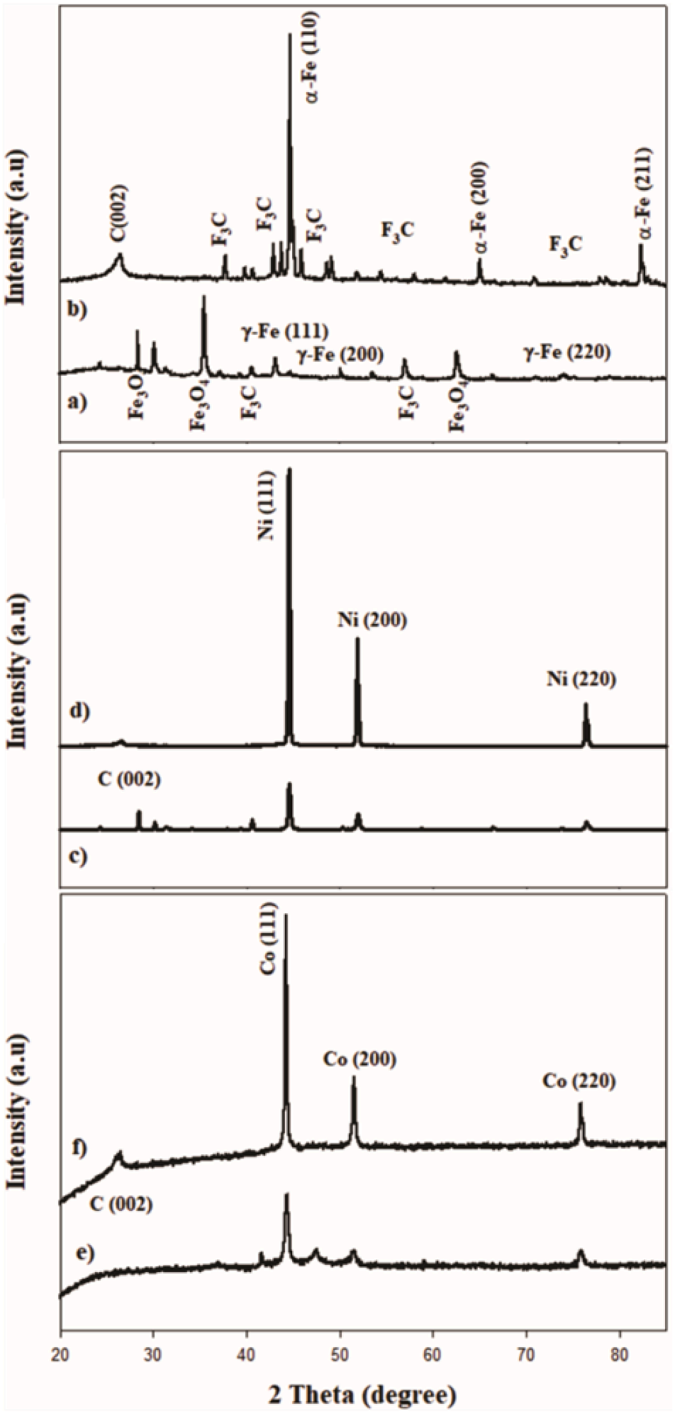

Fig. 3. XRD patterns of **a)** Fe/CA, **b)** N-Fe/CA, **c)** Ni/CA, **d)** N-Ni/CA, **e)** Co/CA, and **f)** N-Co/CA catalysts.

between surface and bulk metal distributions. The higher Ni content in N-Ni/CA may be due to deeper penetration of Ni into the aerogel structure [36]. Differences in sample preparation, washing steps, or losses during synthesis contribute to changes in metal loading. As a result, the Ni in N-Ni/CA catalyst can be detected in higher amounts by ICP-MS compared to the metals in the other catalysts [37]. The results of the XRD, TEM, and XPS analyses of the catalysts can also explain this situation.

The crystal structure of the synthesized electrocatalysts was analyzed using XRD (Fig. 3). A diffraction peak belonging to the C(002) crystal plane of graphitic carbon at the 2θ = 26° angle is more prominent in nitrogen-doped catalysts (PDF # 00–056–0160) [38]. Small peaks around 2θ = 42.5° - 44.5° in the diffractogram of Fe/CA correspond to the diffraction from the Fe(110) plane in the typical cubic spinel structure [39]. Three weak peaks at 2θ = 43.3°, 2θ = 50.2°, and 2θ = 73.7° correspond to the (111), (200), and (220) planes of γ-Fe, respectively (PDF # 98–000–0258). The peaks at 2θ = 40.5° and 2θ = 57.3° are attributed to the (210) and (221) crystal planes of the iron carbide (cementite, Fe_3C) structure (PDF # 00–035–0772) [40]. Distinct peaks at 2θ = 30.1°, 2θ = 35.4°, and 2θ = 62.5° correspond to the (220), (311), and (440) crystal planes of Fe_3O_4 (JCPDS # 88–0866) [41]. Thus, the diffractogram shows that the CA-supported Fe catalyst was oxidized during preparation [42]. The peaks at 2θ = 44.7°, 2θ = 65.0°, and 2θ = 82.3° of the N-Fe/CA catalyst are characteristic of metallic Fe (JCPDS # 87–0721). These distinct peaks correspond to the (110), (200), and (211) crystal planes of body-centered cubic (bcc) α-Fe [43]. The small diffraction peaks are attributed to the small amount of iron carbide (Fe_3C) species formed at the interfaces of metallic Fe nanoparticles and nitrogenated graphitic structure during the heat treatment process (JCPDS # 72–1110) [44]. Strong diffraction peaks at 2θ = 44.5°, 2θ = 51.9°, and 2θ = 76.4° in the case of Ni/CA and N-Ni/CA correspond to the (111), (200), and (220) crystal planes of metallic Ni, respectively [45]. In addition, during nitrogen doping in these catalysts, the face-centered cubic (fcc) Ni metallic form became evident, as indicated by the increase in peak heights, particularly with increasing temperature (JCPDS # 04–0850) [46,47]. Strong diffraction peaks at 2θ = 44.3°, 2θ = 51.5°, and 2θ = 75.8° in the case of Co/CA and N-Co/CA correspond to the (111), (200), and (220) crystal planes of metallic Co, respectively (JCPDS # 15–0806) [38]. The face-centered cubic (fcc) Co metallic form became evident with the increase in peak heights during nitrogen doping, attributed to the rise in temperature [48]. Diffractograms of Fe/CA, Ni/CA, and Co/CA catalysts also exhibited weak diffraction peaks at 2θ = 20°−30°, indicative of crystalline carbon. These crystalline carbon structures weakened and expanded as they turned into amorphous carbon due to heat treatment at high temperatures during nitrogen doping [49]. Diffractograms of the Ni/CA and Co/CA catalysts showed weak diffraction peaks at 2θ values greater than 40° These peaks represent Ni_3C and Co_3C structures, respectively [50]. The intensity of the peaks increased during nitrogen doping, evidencing the growth of metal nanoparticles under the influence of high temperature [51]. This growth is further clearly seen in TEM images. In conclusion, the XRD patterns of the catalysts confirm the observed peaks corresponding to the metallic phase of the respective TMs.

Figure S3 compares FTIR and Raman spectra of Fe/CA, undoped and doped with nitrogen. The FTIR spectrum of Fe/CA displays the vibrational bands that could be attributed to the aerogel's molecule groups: the band at 1630 cm^{-1} corresponding to the stretching of the C=O and C=C, and the bending of N–H, at 1403 cm^{-1} to the bending of C–H, and at 1003 cm^{-1} the bending of the C=C bonds. An additional band at ca. 570 cm^{-1} corresponds to Fe-O stretching vibrations and evidences partial oxidation of Fe. Conversely, no well-defined peaks were observed in the case of N/Fe-CA, evidencing the collapse of the carbon aerogel structure.

Raman spectra of both materials display clear D- and G-bands at ca. 1340 cm^{-1} and 1580 cm^{-1}, respectively, along with a 2D band (or G' band) at ca. 2700 cm^{-1}. The Raman spectrum of N-Fe/CA exhibits an additional band at approximately 662 cm^{-1}, which arises from the presence of Fe. G-band (representative of the vibration of sp^2 hybridized carbon atoms in a graphitic structure) is associated with ordered, crystalline carbon, while D-band is related to the presence of defects or loss of hexagonal symmetry in the carbon structure. The intensity ratio of the D- to the G-band, I_D/I_G, which reflects the graphitic nature of a material (i.e., the degree of imperfection or crystallinity of graphite), differs for the two herein-studied materials. It was determined to be 0.6 and 1 for undoped and nitrogen-doped Fe/CA, respectively. The ratio greater than 1 in the case of N-Fe/CA indicates its amorphous nature. The 2D band provides further information on the number of layers in a graphene

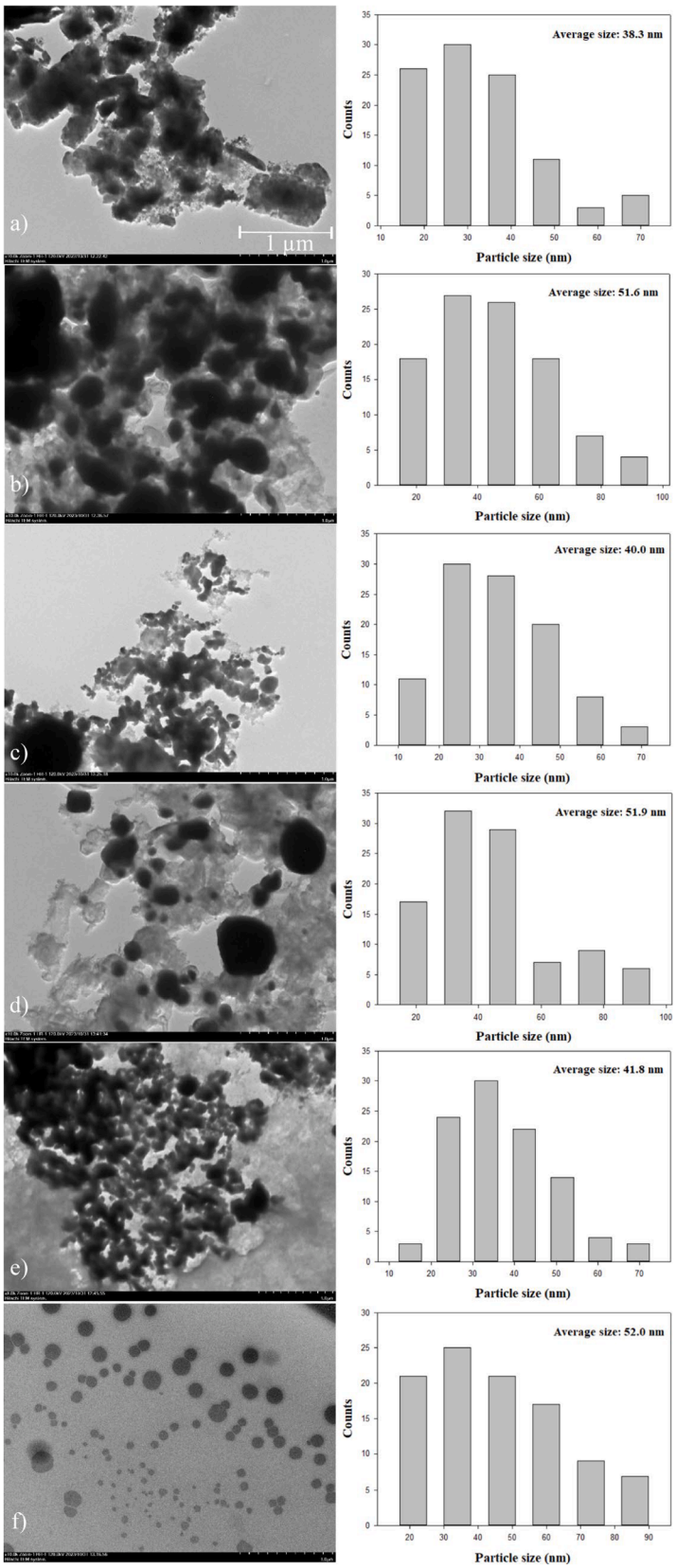

Fig. 4. TEM images (1 μm scale bar) and particle size analyses of **a)** Fe/CA, **b)** N-Fe/CA, **c)** Ni/CA, **d)** N-Ni/CA, **e)** Co/CA, and **f)** N-Co/CA catalysts.

structure, enabling the distinction between monolayer and multilayer graphene. A single, well-defined 2D band observed in the case of Fe/CA suggests a monolayer graphene structure. Conversely, broad peaks with low intensity in the 2D region of N-Fe/CA suggest the presence of multilayer graphene with defects, such as structural or chemical defects.

The average crystallite size of the TMs in the catalysts was calculated using the Debye-Scherrer formula [52] to be > 15 nm (Table 1). High TM loading and the heat treatment step (50 °C for nitrogen-free catalysts and 1000 °C for nitrogenous catalysts) during catalyst synthesis may have increased the possibility of metal nanoparticles agglomerating on the support material. Additionally, the fact that metal particles take different forms during the synthesis also affects the average crystal size. Sun and colleagues synthesized carbon-encapsulated nanoparticles of Fe, Ni, and Co and reported the grain size of the catalysts in the range of 10 - 50 nm. The reason was the formation of carbide phases (Fe_3C, Ni_3Fe, Co_3C) in which carbon atoms transformed into a molten or solid carbon-metal alloy, reflecting the growth history of the nano-encapsulated particles [50].

The crystals of the highest average size belong to Ni/CA and N-Ni/CA catalysts. The average crystal sizes also increased due to nitrogen doping and the high temperature of heat treatment. Sharma et al. examined the effect of carbonization temperature on Ni crystallite size during the synthesis of Ni/C. They reported that the size of almost all Ni particles was > 20 nm at a carbonization temperature of 800 °C. This can be explained by the crystal migration phenomenon and the Tammann temperature. According to the crystal migration phenomenon, metal crystals exhibit surface movements above the Tammann temperature. When these moving crystals collide, they form a larger crystal [53].

TEM images of the synthesized catalysts are given in Fig. 4**.** It can be seen that Fe, Ni, or Co metal particles show dark and light contrast on the CA support material. It is seen that many nanoparticles are positioned on top of each other, have dark contrast, and are embedded in carbonaceous matrices [52]. During the nitrogen doping process to the catalysts, metal particles become unstable due to the increasing temperature. In this case, metal particles tend to come together and agglomerate, thus forming larger particles on the carbon matrix [47].

The TEM image of the N-Co/CA catalyst is different from that of other catalysts. This image shows spherical Co clusters of different sizes distributed on the carbon matrix. Xing et al. encountered a similar morphology of the Co/C catalyst they synthesized. While the size distribution of Co clusters in the Co/C catalyst was 3.5 nm on average, when the material was calcined at 800 °C, some irregular onion-like holes were formed in the flakes, and the average size of Co particles increased to 20 - 30 nm. With a further increase in calcination temperature to 900 °C, the particle size also increased, causing the formation of more onion-like holes in the flakes [54]. Particle size distributions, determined from TEM images at 100 locations and analyzed using ImageJ, are presented in Fig. 4 and Table 1. The average particle size observed in the TEM analysis of the catalysts does not match the average crystal sizes obtained by XRD analysis. A certain heterogeneity in the structure of the catalysts can explain these size differences [55]. However, results should not be directly compared, as XRD cannot detect very small particles and cannot measure the samples' bulk, while TEM analysis provides information on hundreds of particles [56]. The average particle size of the catalysts ranges from 38 to 52 nm. These metal particles show a well-defined core-shell structure of nanoparticles with a shell thickness of approximately 20 nm. Wu and colleagues produced carbon-coated Fe, Ni, and Co nanoparticles (Fe@C, Ni@C, and Co@C) of similar morphology to that observed herein. They reported that Fe@C, Ni@C, and Co@C catalysts comprise spherical particles with sizes ranging from 30 to 60 nm [56]. Additional information on crystal orientation, lattice constants, and defects can be obtained by performing the selected area electron diffraction (SAED) technique [57–59].

The XPS technique was used to analyze the chemical composition, oxidation states, active sites, and electronic environment of the elements present on the surface of CA-supported N-doped Fe, Ni, and Co catalysts.

Table 2
Atomic percentage (data of general spectra) of the elements indicated in the XPS spectra of the catalysts.

Catalyst	at. %			
	TM-$2p_{3/2}$	C 1s	O 1s	N 1s
Fe/CA	1.69	72.35	25.96	–
N-Fe/CA	0.43	93.85	5.00	0.72
Ni/CA	8.68	43.59	47.73	–
N-Ni/CA	1.01	91.02	6.59	1.38
Co/CA	11.11	50.91	37.98	–
N-Co/CA	0.53	94.75	2.93	1.79

General XPS spectra of the catalysts are given in **Figure S2**. Fe 2p, Ni 2p, Co 2p, C 1 s, O 1 s, and N 1 s regions are indicated on the spectra of the catalysts. Data regarding the element types of Fe 2p, Ni 2p, Co 2p, C 1 s, O 1 s, and N 1 s in the spectra (at. %, average positions, and peak areas) are summarized in Table 2 and **Table S1**. In N-Fe/CA, N-Ni/CA, and N-Co/CA catalysts, C 1 s at. % ratios and peak areas are increased significantly, and O 1 s at. % ratios and peak areas are decreased. This situation demonstrates that oxygen is removed during pyrolysis, a process in which nitrogen doping occurs. It is observed that TM-$2p_{3/2}$ at. % ratios, which also occur with the weakening of the metal signal in the XPS analysis after nitrogen doping, have decreased. This situation is due to the more homogeneous distribution of metal nanoparticles in the carbon matrix [60]. After nitrogen doping, the N 1 s peak is observed in the spectra. This indicates that successful nitrogen doping has been achieved. The highest N doping rate was achieved with the N-Co/CA catalyst at 1.79 at. %.

Partial spectra of XPS analyses help to determine binding energy shifts that indicate chemical bonding and oxidation states. Fe 2p, Ni 2p, Co 2p, C 1 s, O 1 s, and N 1 s partial spectra of nitrogen-doped catalysts are given in **Figure S3,** while the partial spectra of non-doped catalysts are given in Fig. 5. The binding energies corresponding to the peaks, chemical bonds, and the percentage ratios of the element types belonging to the bonds are also indicated in these spectra. The apparent binding energies in the TM 2p partial spectra of the catalysts are summarized in Table 2. The regions of Fe $2p_{3/2}$, Fe $2p_{1/2}$, and their satellites represent the Fe^{3+} element type (Fe_2O_3, FeOOH, or complex Fe-N structures) [26]. The regions of Ni $2p_{3/2}$, Ni $2p_{1/2}$, and their satellites represent the Ni^{2+} element type (NiO, $Ni(OH)_2$, or Ni-N_x structures) [24]. The regions of Co $2p_{3/2}$, Co $2p_{1/2}$, and their satellites represent the Co^{3+} and Co^{2+} element types (Co_3O_4, CoO, or Co-N_x structures), respectively [61]. In the C 1 s partial spectra of the catalysts, metal-carbide bonds (Fe-C, Co-C, Ni-C) formed by the interaction of TMs with CA, graphite-like sp^2 carbon bonds (C=C), oxidized carbon species (O-C=O), π–π^* interactions in graphitic carbons are clearly shown [62]. Co/CA catalyst contains more oxide forms than the others. As a result of N doping, graphitic forms in the catalyst's structure increased due to the effect of pyrolysis. In the O 1 s partial spectra of the catalysts, the forms of metal oxides representing metal-O bonds (Fe_2O_3, CoO, NiO), surface hydroxyl groups (-OH), and surface adsorbed water (H_2O) are clearly visible [25]. As a result of N doping, the adsorbed H_2O in the structure of the catalysts decreased due to the effect of pyrolysis. The N 1 s spectrum of the catalysts contains different peaks depending on the chemical environment of N and metal-N-C interactions. N species are in the forms of pyridinic-N (398.0–398.6 eV) which contributes to the formation of Fe-N_x, CoN_x, Ni-N_x structures that form active sites for ORR and OER activities, pyrrolic-N (399.0–399.6 eV) which provides pseudocapacitance contribution in supercapacitor applications, graphitic-N (400.5–401.0 eV) or quaternary-N (~401.0–402.0 eV), which increase electrical conductivity and contribute to the stability of the material, oxidized pyridinic-N or oxidized-N (402.0–408.0 eV) which cause decrease in conductivity with surface oxidation and sometimes form hydrophilic surfaces [63,64]. Metal-N_x bonds were formed in all N-doped catalysts. In addition, in the N-Co/CA catalyst, unlike the

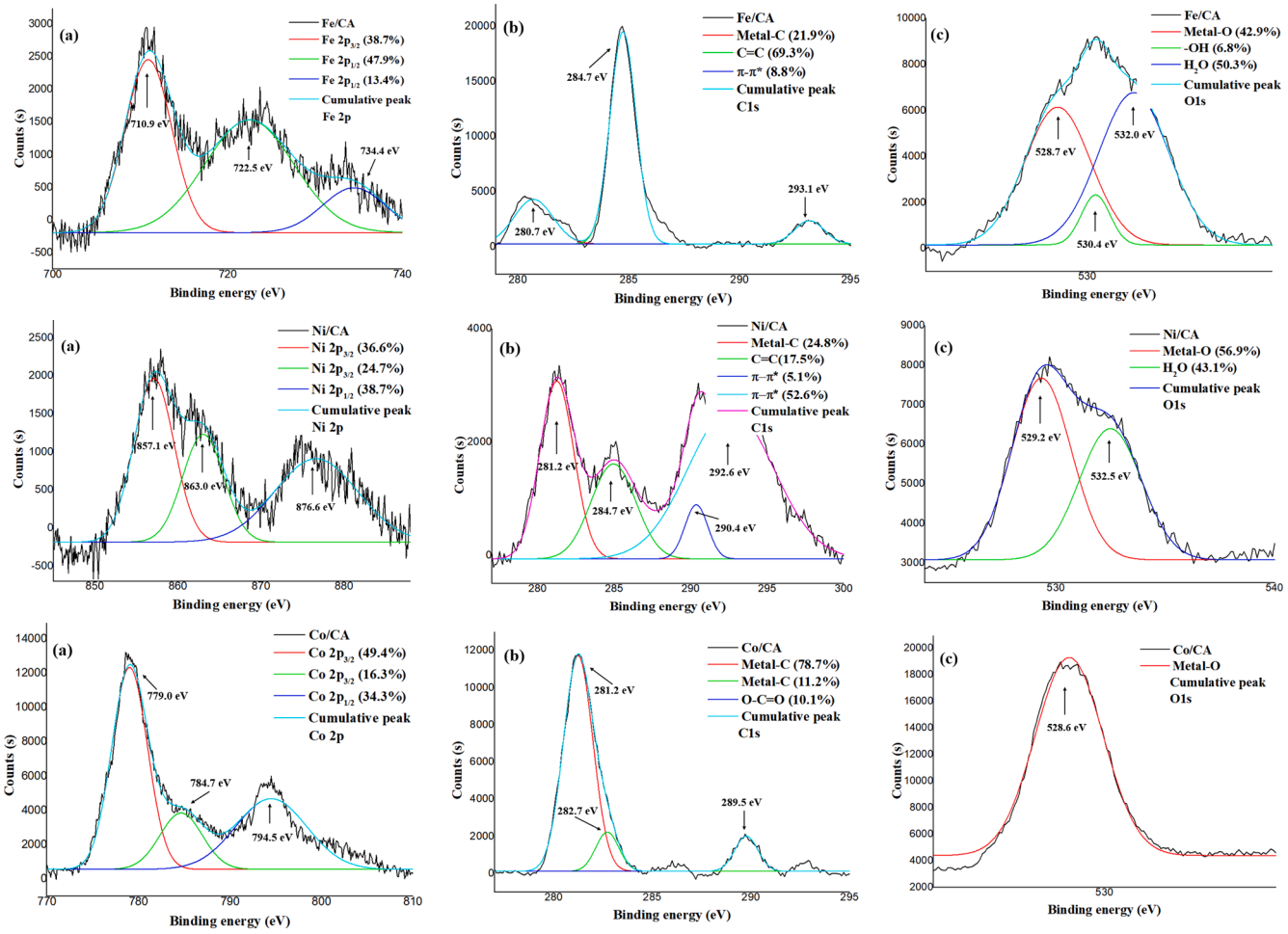

Fig. 5. XPS partial spectra of Fe/CA, Ni/CA, and Co/CA catalysts: **a)** TM - 2p, **b)** C 1 s, **c)** O 1 s.

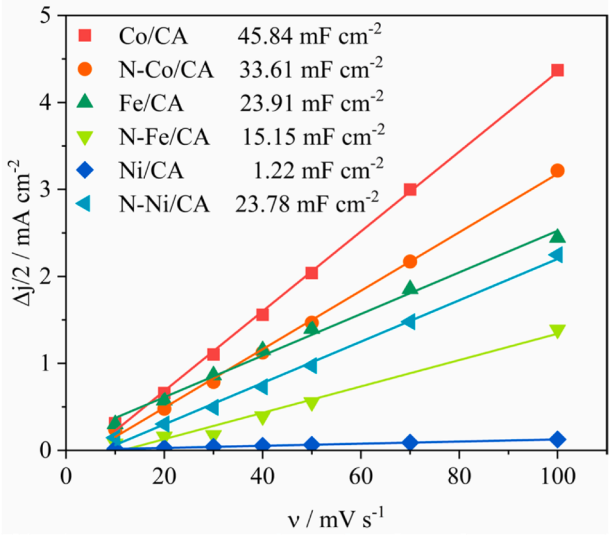

Fig. 6. Δj/2 vs. scan rate plots of the studied catalysts and the corresponding C_{dl} values.

others, graphitic-N type was formed, which positively affected the catalytic performance.

3.2. *Double-layer investigation*

Electrochemical analysis of the materials was performed in a setup described in the Supplementary Information file. The mass loading of the active material was adjusted to approximately 0.5 mg cm^{-2}, which is lower than the value suggested in the literature for supercapacitor applications [65,66]. However, thin catalyst films were used to avoid excessive material loading and related issues such as mass transport limitations within the catalyst layer, increased ohmic drop, and mechanical instability.

Investigation of double-layer capacitance (C_{dl}) can provide insight into the electrochemically active surface area (ECSA) of each catalyst. The C_{dl} is strongly influenced by multiple parameters, including electrode potential, surface morphology, electrolyte composition, and ionic strength; consequently, subtle alterations in these variables can significantly affect the measured capacitance. C_{dl} was investigated by recording a series of CVs in the non-Faradaic potential region (**Figure S4**) at different scan rates. Subsequently, $\Delta j/2 = f(\nu)$ was plotted (Fig. 6), where $\Delta j = (j_a - j_c)$, and j_a and j_c are the anodic and cathodic current values, respectively, at the chosen halfway potential, and ν is the scan rate of the electrode potential. C_{dl} can then be determined as the slope of the $\Delta j/2 = f(\nu)$ plot from which ECSA is determined as C_{dl}/C_{ref}. It was assumed that C_{ref} = 40 μF per cm^2 of the geometric surface area, which is the most common value used in the literature for alkaline electrolytes [67]. Quantification of the ECSA via

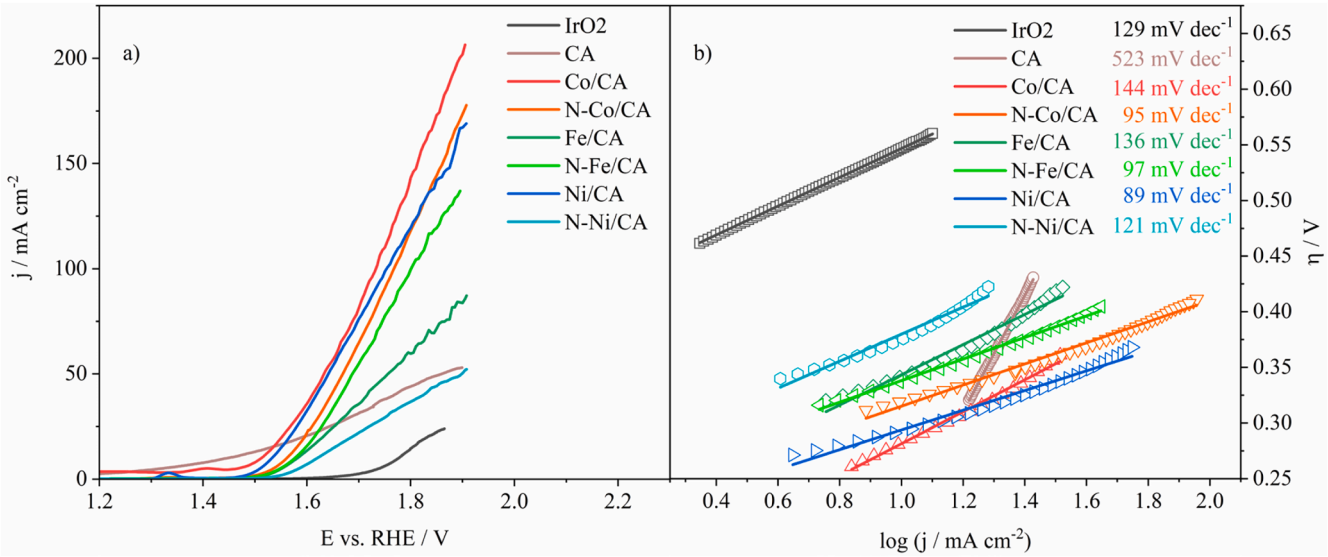

Fig. 7. a) LSVs (iR-corrected) in 1 M KOH at 10 mV s^{-1} and **b)** Tafel analysis for the studied catalysts.

Table 3
Comparison of OER parameters of the herein prepared electrocatalysts and similar electrocatalysts reported in the literature.

Sample	η_{10} (mV)	j_{400} (mA cm^{-2})	Tafel slope (mV dec^{-1})	E_{onset} (V vs. RHE)	Source
CA	219	23.5	523	1.35	This work
Co/CA	276	53.4	144	1.49	This work
N-Co/CA	316	37.3	95	1.54	This work
Fe/CA	341	22.7	136	1.55	This work
N-Fe/CA	336	29.7	97	1.55	This work
Ni/CA	291	49.6	89	1.50	This work
N-Ni/CA	381	13.2	121	1.56	This work
IrO_2	378	20.6	129	1.69	This work
Co/N-C-800	371	–	61.4	–	[68]
Co/gCN-MWS	451	–	78.4	1.52	[69]
Co-SA@NCA	400	–	–	–	[17]
Fe/C	370	–	102	–	[70]
Fe NC@NSCA	400	–	102	1.56	[18]
Ni/C	330	–	121	–	[70]
Ni-SA@NCA	380	–	90	1.51	[17]
Ni NP@NSCA	370	–	82	1.54	[18]

*N-C-800 – nitrogen-doped carbon at 800 °C, gCN-MWS – graphitic carbon nitride obtained by microwave synthesis, SA – single atom, NCA – nitrogen-doped carbon aerogel, NC@NSCA – nanoclusters anchored on nitrogen and sulfur co-doped with carbon aerogel.

measurements conducted within the non-Faradaic potential region, thus avoiding polarization into the oxygen evolution range, circumvents complications associated with surface-altering processes (oxide formation or metal dissolution/redeposition). As a non-destructive technique, it allows for the evaluation of the total surface area accessible to the electrolyte. However, in systems where metallic particles are dispersed within an inert matrix, such as the case of TM on CA, the measured value corresponds to the overall surface area rather than the active area of the metallic phase. While this approach does not offer the accuracy or rigor of more established methodologies, it remains valuable for estimating and comparing the ECSA of compositionally or structurally similar materials, such as those examined in the present study.

The pure, undecorated CA exhibited a C_{dl} of 40.39 mF cm^{-2}, corresponding to an ECSA of 1010 cm^2. Investigation of the decorated materials revealed that the highest C_{dl} and, subsequently, the highest ECSA were achieved for Co/CA, with values of 48.84 mF cm^{-2} and 1146 cm^2, respectively. Slightly lower values were calculated for N-Co/CA (33.61 mF cm^{-2} with an ECSA of 840 cm^2), while Fe/CA and N-Ni/CA with C_{dl} of 23.91 and 23.78 mF cm^{-2} and ECSA of 598 and 595 cm^2, respectively, had almost two times lower values than Co/CA. C_{dl} calculated for N-Fe/CA was 15.15 mF cm^{-2}, which corresponds to an ECSA value of 379 cm^2. The lowest value of C_{dl} was calculated for Ni/CA, 1.22 mF cm^{-2}, with an ECSA value of 30 cm^2. All calculated C_{dl} and ECSA values are summarized and compared in **Table S2**.

3.3. *Electrocatalytic activity for OER*

Fig. 7 depicts the LSVs for the prepared catalysts under OER conditions in alkaline medium. Co supported on CA exhibits the highest electrocatalytic activity towards OER, driving current densities of 200 mA cm^{-2} at 1.9 V. Conversely, N-Ni/CA shows the lowest performance with a current density of 50 mA cm^{-2} at the same potential. Three key OER parameters were evaluated, enabling the proper comparison of electrocatalysts: the overpotential required to reach a current density of 10 mA cm^2 (η_{10}), the current density at an overpotential of 400 mV (j_{400}), and the Tafel slope (b). The OER data are summarized in Table 3 and compared with the values reported in the literature for similar OER catalysts. Co/CA reaches 10 mA cm^{-2} at the lowest overpotential of 276 mV with a Tafel slope of 144 mV dec^{-1}, indicating its high catalytic activity for the OER. Moreover, η_{10} of Co/CA is 100 mV lower than that of the state-of-the-art IrO_2 electrocatalyst (378 mV), which was tested under the same conditions. Accordingly, the current density at an overpotential of 400 mV delivered by Co/CA (53.4 mA cm^{-2}) was more than 2.5 times higher than that of IrO_2 (20.6 mA cm^{-2}). Another type of cobalt-doped aerogel (Co/N-C-800) [68] and Co supported on graphitic carbon nitride obtained by microwave synthesis (Co/gCN-MWS) [69] were reported with higher overpotential to achieve 10 mA cm^{-2} and relatively small Tafel slope (Table 3).

Besides Co/CA, good catalytic activity was also observed for Ni/CA and N-Co/CA, which have reached similar current densities at 1.9 V (≈ 175 mA cm^{-2}) with overpotential to achieve 10 mA cm^{-2} of 291 mV and 316 mV, respectively, lower than N-Fe/CA (336 mV), Fe/CA (341 mV), and N-Ni/CA (381 mV). Furthermore, Ni/CA and N-Co/CA also showed higher current densities delivered at an overpotential of 400 mV as well as lower values of Tafel slope (89 and 95 mV dec^{-1}, respectively) compared with N-Fe/CA, Fe/CA and N-Ni/CA (97, 136, and 121 mV dec^{-1}, respectively), as well as Co/CA (144 mV dec^{-1}). It is worth mentioning that the pure, undecorated CA also exhibited a low onset potential for OER and a low overpotential to reach a current density of

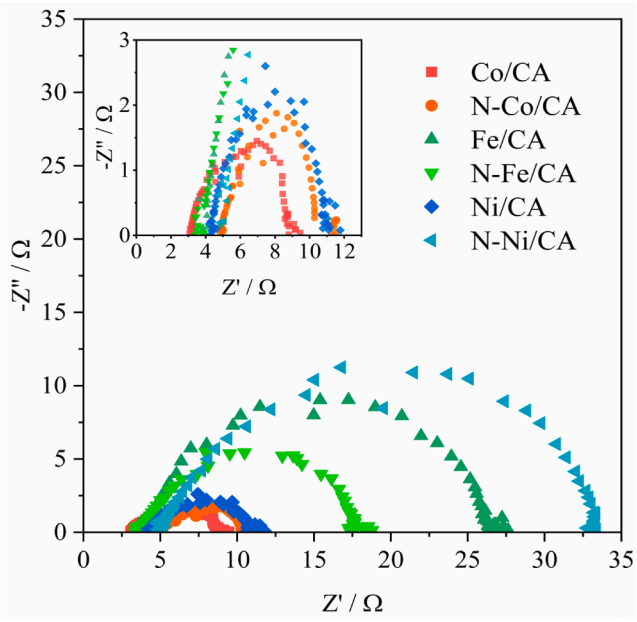

Fig. 8. Nyquist plots for the studied catalysts at 1.7 V in 1 M KOH.

10 mA cm^{-2}. However, a very high Tafel slope of 523 mV dec^{-1} and the low overall achieved current density within the investigated potential window compared to the rest of the studied materials indicate that the CA is better suited as a supporting material for transition metal nanoparticles, rather than as a standalone OER catalyst.

Nyquist plots at 1.7 V presented in Fig. 8 illustrate the charge-transfer resistance, R_{ct}, of each catalyst during OER catalysis. Both thermodynamic and kinetic constraints limit the OER. Density functional theory calculations have revealed intrinsic relationships between the adsorption energies of key intermediates such as *OH and *OOH. The sequential, multi-electron nature of OER, involving the mentioned intermediate species (*OH, *O, and *OOH), contributes to substantial activation energy barriers that challenge the reaction kinetics. The complex mechanism, encompassing both the adsorbate evolution mechanism and the lattice oxygen mechanism, results in the rate-determining step's dependence on the catalyst and electrolyte environment.

The high-frequency intersection with the Z'-axis of Nyquist plots represents R_s, the sum of the resistances of electrolyte, electrode material, and wiring in the system. At the same time, the R_{ct} is calculated as the low-frequency intersection with the Z'-axis from which R_s is subtracted. A clearly defined semicircle is observed for all investigated catalysts, corresponding to the one-phase angle maxima at lower frequencies, and it can be attributed to the adsorption of OER intermediates on the electrode. Co/CA shows the smallest semicircle in these Nyquist plots, corresponding to the smallest R_{ct} of 5.49 Ω and, consequently, the fastest charge transfer during the O_2 evolution process.

Similar R_{ct} values (**Table S3**) were calculated for N-Co/CA and Ni/CA (5.51 Ω and 6.69 Ω), respectively. In contrast, Fe/CA, N-Fe/CA, and N-Ni/CA showed higher R_{ct} values, indicating that the OER kinetics on these materials are mainly controlled by the charge-transfer process. Furthermore, partially flattened semicircles in Nyquist plots indicate the existence of dispersive capacitance [71].

The stability of Ni/CA and Co/CA under OER conditions, as another crucial electrocatalyst's characteristic, was probed using chronoamperometry at 1.7 V. These experiments revealed excellent stability of both investigated materials. A comparison of LSVs before and after the stability test (Fig. 9) illustrates an increase in current density after the test. The current density increased by 24 % and 33 % for Co/CA and Ni/CA, respectively. Ni-Co phosphate nanocages supported by wastepaper-based carbon aerogels (NCP@WPCA) studied for OER revealed good stability in alkaline solution with an overpotential of 351 mV at 10 mA cm^{-2} [11]. Herein, an overpotential of 290 mV and 330 mV at 10 mA cm^{-2} was determined for Co/CA and Ni/CA, respectively, after the stability test. The overpotential to reach 50 mA cm^{-2} decreased after the stability test by ca. 30 mV in the case of Co/CA (from 380 mV to 350 mV) and by ca. 50 mV in the case of Ni/CA (from 470 mV to 420 mV). Moreover, Tafel slope values decreased from 125 mV dec^{-1} to 94 mV dec^{-1}, and from 110 mV dec^{-1} to 92 mV dec^{-1} for Co/CA and Ni/CA, respectively, after the stability test. The observed increase in current density and decrease in overpotential suggest an increased availability of active centers, resulting from the enhanced diffusion of electrolyte into CA pores over time.

Overall, in the C_{dl} analysis, the highest ECSA was observed for Co/CA, followed by N-Co/CA, Fe/CA, etc. Co/CA also proved to be the best in OER catalysis mode, achieving the highest overall current density and the lowest overpotential to reach 10 mA cm^{-2}, which is lower than that of IrO_2 tested under the same conditions. However, the trend observed in the C_{dl} investigation, namely the decrease of ECSA value from Co/CA to Ni/CA, cannot be related to OER catalysis results. Ni/CA, which had

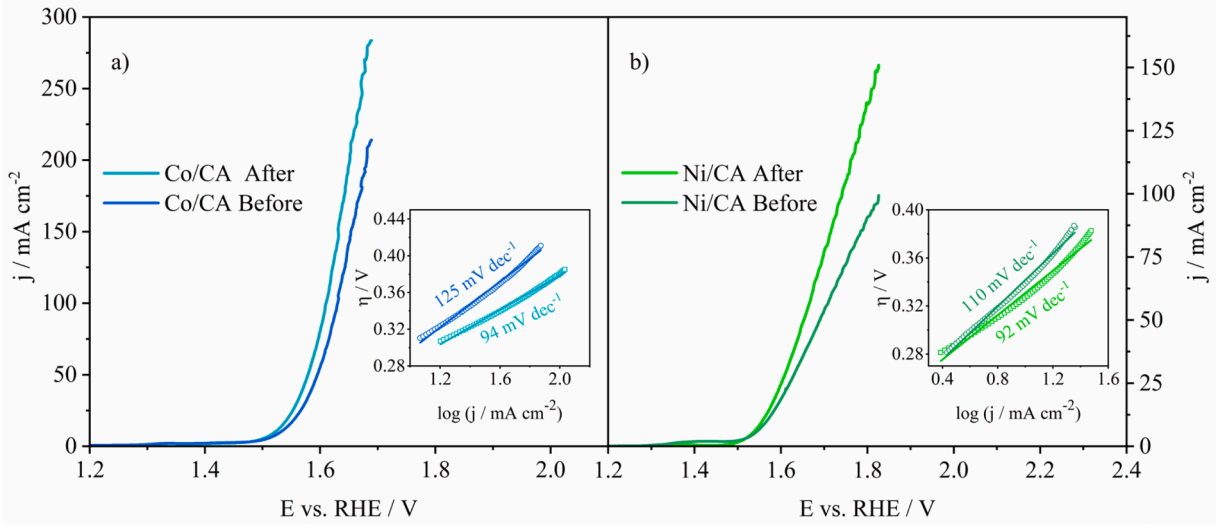

Fig. 9. LSVs (iR-corrected) of **a)** Co/CA and **b)** Ni/CA in 1 M KOH at 10 mV s^{-1} before and after stability tests performed during 4 h with the corresponding Tafel plots in the inset.

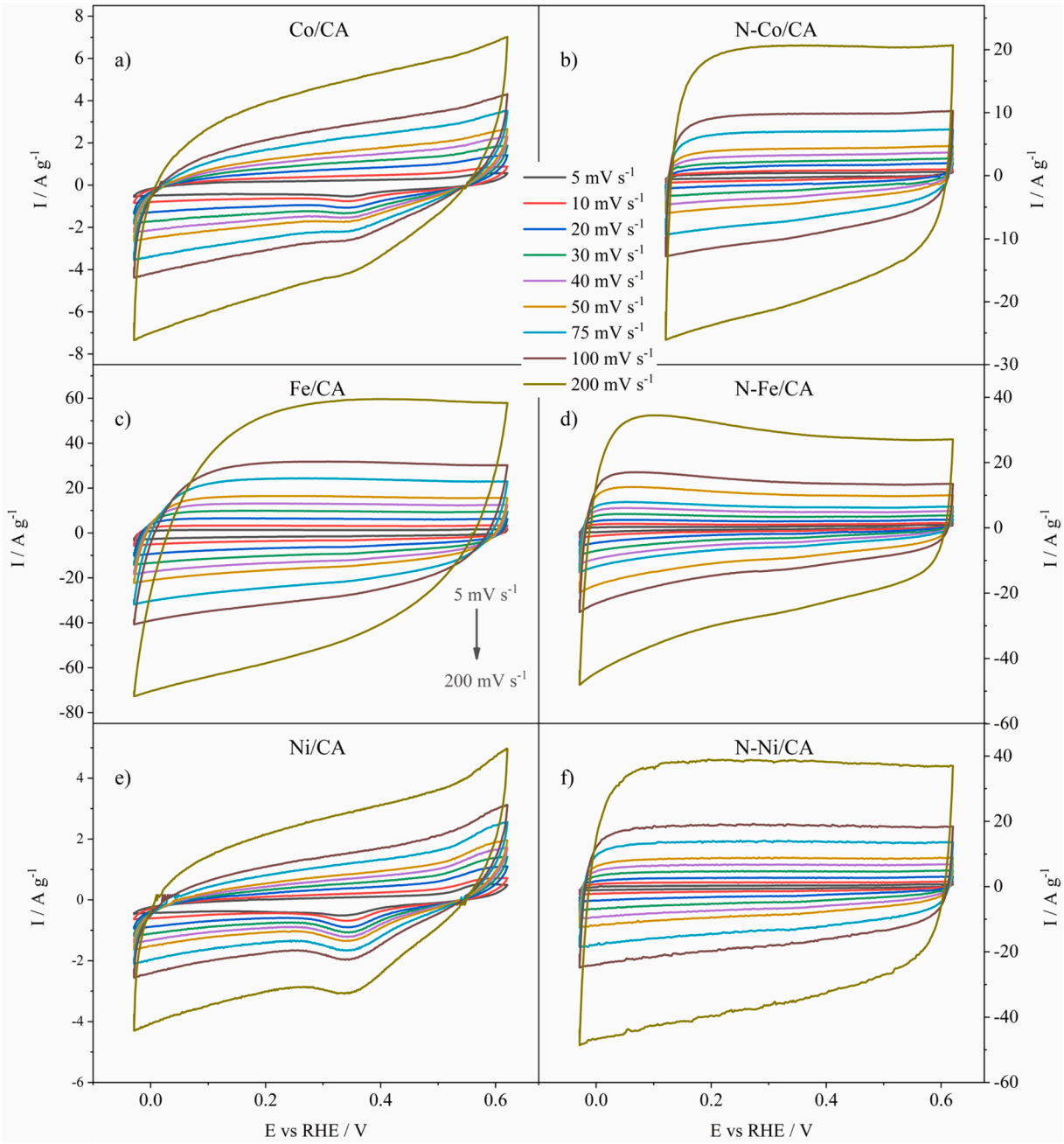

Fig. 10. CVs of the studied materials in 3 M KOH at different scan rates.

the lowest value of ECSA, also performed as the second best for OER catalysis, suggesting that other factors play a role in catalysis of OER, including the size of metal particles, their oxidation state, and accessibility. OER is generally favored by the active sites in higher oxidation states compared to metallic forms, with the latter being present in higher amounts in the case of the three catalysts with incorporated nitrogen. Still, introducing nitrogen into TM/CA did not bring the expected enhancement of their electrocatalytic activity, possibly due to the agglomeration of nanoparticles during the doping heat treatment. Moreover, the collapse of the carbon 3D structure occurred during the treatment, reflecting on the ability of ions to travel to/from the active sites.

3.4. Capacitance measurements

The specific capacitance, C_s, of the studied materials was calculated from their cyclic voltammograms recorded in a 3 M KOH solution at different scan rates (Fig. 10**)** using Eq. S1. The CVs of the undecorated CA are shown in **Figure S5**. It should be noted that the electrode tested for supercapacitor applications was prepared using three additional loadings (0.25, 0.85, and 9 mg cm^{-2}) with specific current densities and accumulated charge decreasing as the loading increased **(Figure S6**). A loading of ca. 0.5 mg cm^{-2} was selected to balance the activity and mass loading.

The CV curves presented a rectangular shape, suggesting an electrical double-layer capacitive (EDLC) behavior. CV curves of Co/CA and Ni/CA also exhibited a redox peak in the 0.3 - 0.4 V region due to Faradaic processes. Fe/CA delivered a significantly higher C_s compared to N-Fe/CA and N-Ni/CA, which showed similar results (Fig. 10**a**). This can be attributed to the facile electrolyte ion diffusion associated with the 3D structure of Fe/CA. At 20 mV s^{-1}, the C_s values were determined to be 298, 174, and 171 F g^{-1} for Fe/CA, N-Fe/CA, and N-Ni/CA,

Table 4
Specific capacitance, C_s, and specific energy, E_s, of the studied materials calculated from the CVs at 20 mV s^{-1} and compared with literature data.

Sample	C_s / F g^{-1}	E_s / Wh kg^{-1}	Source
CA	269	78.22	This work
Co/CA	35	10.86	This work
N-Co/CA	86	13.40	This work
Fe/CA	298	87.98	This work
N-Fe/CA	174	31.80	This work
Ni/CA	20	6.82	This work
N-Ni/CA	171	38.80	This work
$NiCo_2S_4$	–	12.32	[75]
Co-doped MnO_2 nanocomposite	338	–	[76]
Bio-CAA/CNT/CNF	481	39.63	[77]
GD-doped carbon aerogels	180	6.30	[78]
MnO_2-graphene aerogels	284	10.0	[79]
NSCA	249	26.15	[80]

CAA/CNT/CNF – carbon aerogel/carbon nanotube/cellulose nanofiber; GD - graphene dots; NSCA – nitrogen self-doped carbon aerogels.

respectively (Table 4). The high C_s values determined for Fe/CA in alkaline media are consistent with what is reported in the literature for CA materials [72,73]. For example, nanocellulose-based CAs delivered C_s values of 205 and 302 F g^{-1} in alkaline solution [73]. On the other hand, the nickel cobaltite/carbon aerogel composite exhibited ultrahigh C_s values of approximately 1700 F g^{-1} in 1 M NaOH media [72].

N-Co/CA, Co/CA, and Ni/CA showed significantly lower C_s compared to Fe/CA, N-Fe/CA, and N-Ni/CA. For N-Co/CA, the C_s was determined to be 86 F g^{-1} at 20 mV s^{-1}, while Co/CA and Ni/CA showed even lower values of 35 and 20 F g^{-1}, respectively. This is opposite to the results acquired with the same materials when tested for OER catalysis, where Co/CA and Ni/CA showed the highest activity.

N-doping of the catalyst has been reported to facilitate pseudo-Faradaic processes, thus increasing the amount of charge that can be stored [74]. For N-Co/CA and N-Ni/CA, an increase in total capacitance is evident (Figs. 10**b,f**) compared to non-N-doped materials (Figs. 10**a, e**), while the same effect is not observed in the case of Fe/CA catalyst doping (Figs. 10**c,d**). However, all three N-doped catalysts showed evidence of easier polarization, as manifested in swifter current switching at vertex potentials and a nearly horizontal orientation. The additional electrons provided by electron-rich nitrogen to the sp2/sp3 hybridized carbon backbone ensure no significant ohmnic drop in the CVs of these materials. In contrast, the CVs of all three non-N-doped catalysts were distorted, indicating significant ohmic resistance and a sluggish current response at switching potentials [74]. This type of behavior of non-N-doped catalysts is probably due to the lack of electrons from nitrogen and an overly porous structure, which can limit the polarization of parts of the material surface, preventing them from participating in charge storage and consequently lowering the capacitance values [74].

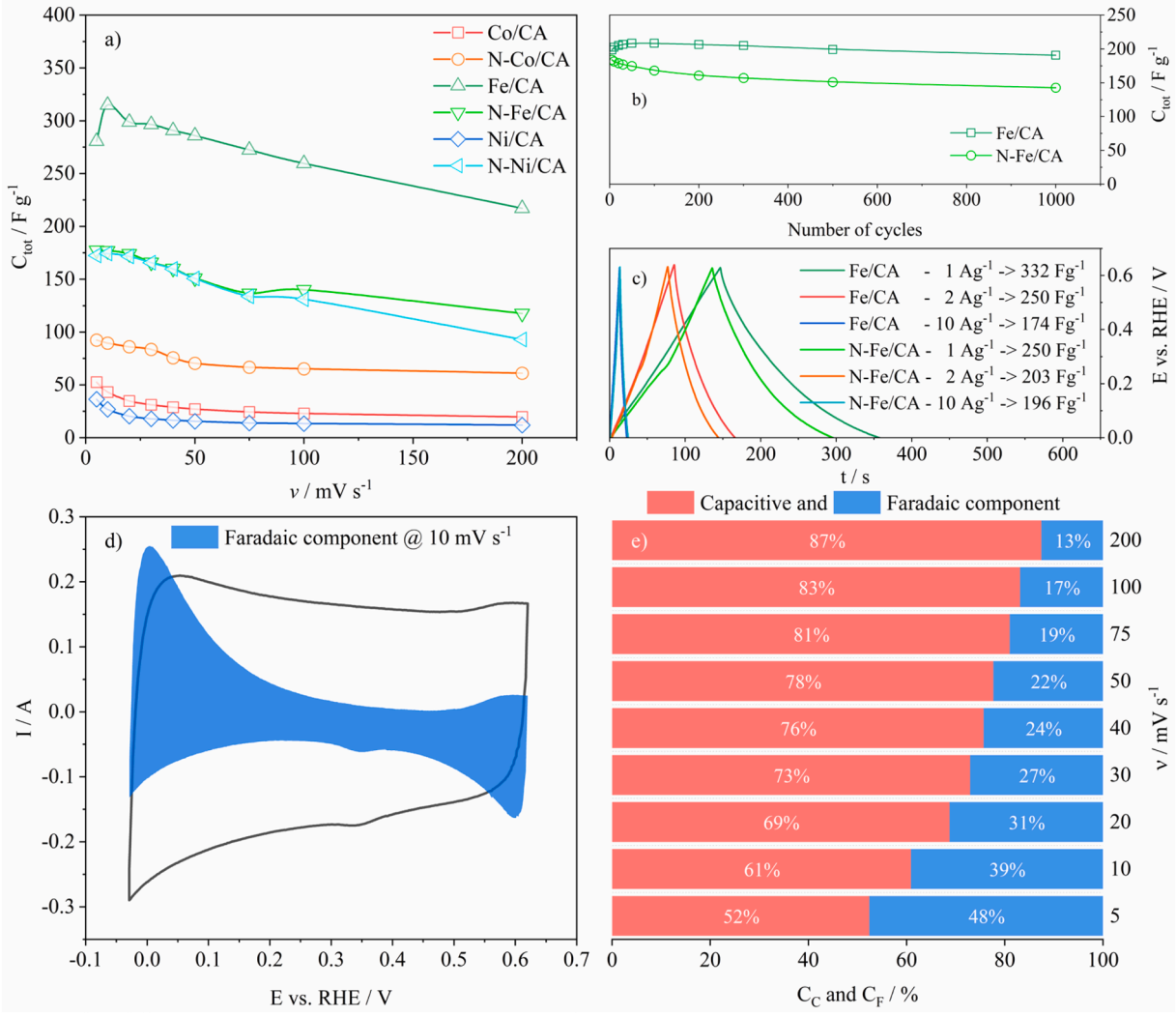

Fig. 11. a) Dependence of specific capacitance on the scan rate of the electrode potential, **b)** cycling stability, **c)** galvanostatic charge-discharge curves at different specific currents, **d)** contribution of Faradaic component to overall capacitance for Fe/CA, and **e)** Dunn analysis for Fe/CA at different scan rates.

A comparison between the supercapacitive performance of the synthesized composites and pure CA revealed that only Fe/CA outperforms pure CA in terms of C_s value, as shown in Table 4. Therefore, the strategy used to introduce selected transition metals may not be optimal for enhancing charge storage ability. The high metal content in the composite (up to 70 wt. % in the case of Ni) and metal agglomeration may block voids and highly active sites on the carbon, reducing the energy density of the carbon supercapacitor.

Fig. 11**a** depicts the dependence of the total capacitance on the scan rate for the tested materials. As expected, total capacitance decreases with increased scan rate for all materials. This decrease in capacitance is well-documented and is often attributed to the electrical resistance of the active material [81,82]. However, as discussed earlier, the introduction of heteroatoms can reduce the resistance of the materials [74, 81,82]. This phenomenon is also observed in catalysts doped with nitrogen, which exhibited a slightly smaller reduction in total capacitance as the scan rate increased compared to non-doped catalysts.

The stability of the best-performing Fe/CA during the prolonged cycling in 3 M KOH at 100 mV s^{-1} is depicted in Fig. 11**b,** along with the stability of nitrogen-doped N-Fe/CA under the same experimental conditions. It can be seen that the C_s of Fe/CA increases slightly in the first 50 cycles (approximately 5 %), followed by a gradual decrease to 96 % of its initial capacitance after 1000 cycles, indicating excellent stability of the material. In the case of nitrogen-doped N-Fe/CA, an initial increase is not observed; instead, a steady decrease in the C_s from its initial value of 184 F g^{-1} to 143 F g^{-1} (decrease of ~23 %), indicating somewhat lower stability of the doped material.

Fig. 11**c** depicts the galvanostatic charge-discharge (GCD) curves of Fe/CA and nitrogen-doped N-Fe/CA under different current loads (1, 2, and 10 A g^{-1}) in a three-electrode setup. Fe/CA delivered a C_s (Eq. S2) of 322 F g^{-1} under the moderate load of 1 A g^{-1}, while N-Fe/CA delivered 250 F g^{-1}. Further increasing the current load to 2 and 10 A g^{-1} resulted in a decrease in capacitance to 250 and 174 F g^{-1} for Fe/CA, and to 203 and 196 F g^{-1} for N-Fe/CA, respectively. The results obtained are comparable to those reported in the literature. For instance, Co-doped@MnO_2 delivered a C_s of 337.8 F g^{-1} at 0.5 A g^{-1} [76]. On the other hand, nano-flake-rod-like CoMoO–S supported Ni-foam and cactus-like Ni-Co/$CoMn_2O_4$ composites on Ni foam delivered significantly higher C_s of 1087 F g^{-1} at 2 A g^{-1} and 1567 F g^{-1} at 0.5 A g^{-1}, respectively [83, 84].

Figs. 11**d** and 11**e** represent Dunn's analysis of the best-performing Fe/CA material for scan rates from 5 to 200 mV s^{-1}. The capacitive contribution increases from 52 % at lower scan rates, where charge accommodation is better defined in the material, to 87 % at 200 mV s^{-1}, where the Faradaic contribution is significantly lower. Furthermore, the Faradaic component at lower scan rates shows distinctive maxima, which are attributed to Fe redox processes.

The TM/CA catalysts developed in this study demonstrated notable improved performance compared to those reported in the literature. For OER electrocatalysis, Co/CA required an overpotential of only 276 mV at 10 mA cm^{-2}, which is lower than that of the benchmark IrO_2 catalyst, while also exhibiting a relatively small Tafel slope of 110 mV dec^{-1} and excellent long-term stability, with catalytic activity increasing during extended operation. These features represent a significant advancement over many transition-metal-based catalysts, which typically exhibit higher overpotentials and degradation in performance over time. In terms of supercapacitor applications, Fe/CA delivered a C_s of 322 F g^{-1} at 1 A g^{-1}, comparable to, for example, Co-doped MnO_2 (337.8 F g^{-1} at 0.5 A g^{-1}) [76]. Although the capacitance values are lower than some reported [83,84], Fe/CA exhibited exceptional cycling stability, retaining 96 % of its capacitance over 1000 cycles, which is superior to many high-capacitance systems that often compromise stability. Importantly, the dual applicability of the TM/CA catalysts in both OER electrocatalysis and supercapacitor energy storage underscores their versatility and, along with their cost-effectiveness, provides a promising alternative to existing state-of-the-art materials.

4. Conclusions

This study involved the preparation of three transition metals supported on carbon aerogel, both undoped and doped with nitrogen, and their evaluation as electrode materials for the oxygen evolution reaction and supercapacitors in alkaline media. The materials exhibited a moderate degree of porosity, with a dominant microporous structure with some mesopores present. Undoped TM/CA catalysts comprised crystalline carbon; however, they turned into amorphous carbon during nitrogen doping due to the heat treatment. Additionally, metal particles agglomerated during the doping process. The best OER catalytic performance was observed with Co/CA and Ni/CA, which required low overpotentials of 276 and 291 mV, respectively, to reach 10 mA cm^{-2}, with Tafel slopes of 144 and 89 mV dec^{-1}. Co/CA exhibited the highest electrochemically active surface area of 1146 cm^2 and the lowest charge-transfer resistance of 5.5 Ω, which contributed to its high catalytic performance. Both catalysts performed exceptionally well during the extended cycling stability test, with their activity increasing over time.

Regarding the potential of TM/CA and N-TM/CA as supercapacitor electrodes, Fe/CA exhibited the highest specific capacitance of 298 F g^{-1} at 20 mV s^{-1} and demonstrated excellent stability throughout the 1000-cycle test, with a capacitance decrease of only 4 %. Fe/CA also exhibited a notable specific capacitance of 322 F g^{-1} during the galvanostatic charge-discharge at 1 A g^{-1}, further confirming its high performance.

CRediT authorship contribution statement

Dušan Mladenović: Writing – original draft, Visualization, Investigation, Formal analysis, Data curation. **Marta Martins:** Writing – original draft, Visualization, Investigation, Formal analysis. **Meryem Samancı:** Writing – original draft, Visualization, Investigation, Formal analysis, Data curation. **Miguel Charneca:** Visualization, Investigation, Formal analysis. **Anup Paul:** Writing – original draft, Visualization, Investigation, Formal analysis. **Diogo M.F. Santos:** Writing – review & editing, Supervision, Conceptualization. **Ayşe Bayrakçeken:** Writing – review & editing, Supervision, Conceptualization. **Biljana Šljukić:** Writing – review & editing, Supervision, Project administration, Funding acquisition, Conceptualization.

Declaration of competing interest

The authors declare that they have no known competing financial interests or personal relationships that could have appeared to influence the work reported in this paper.

Acknowledgements

The authors would like to thank the Ministry of Science, Technological Development and Innovation of the Republic of Serbia (contract no. 451–03–136/2025–03/200146 and 451–03–137/2025–03/200146), as well as Fundação para a Ciência e a Tecnologia, Portugal, for funding a Principal Researcher contract (2023.09426.CEECIND, doi:10.54499/2023.09426.CEECIND/CP2830/CT0021) in the scope of the Individual Call to Scientific Employment Stimulus - 6th Edition (D. M.F.S).

Supplementary materials

Supplementary material associated with this article can be found, in the online version, at doi:10.1016/j.electacta.2025.147226.

Data availability

Data will be made available on request.

References

[1] J. Jin, J. Yin, H. Liu, M. Lu, J. Li, M. Tian, P. Xi, Transition metal (Fe, Co, and Ni)–carbide–nitride (M–C–N) nanocatalysts: structure and electrocatalytic applications, ChemCatChem. 11 (2019) 2780–2792, https://doi.org/10.1002/cctc.201900570.

[2] L. Han, S. Dong, E. Wang, Transition-metal (Co, Ni, and Fe)-based electrocatalysts for the water oxidation reaction, Adv. Mater. 28 (2016) 9266–9291, https://doi.org/10.1002/adma.201602270.

[3] T. Asefa, X. Huang, Heteroatom-doped carbon materials for electrocatalysis, Chem. Eur. J. 23 (2017) 10703–10713, https://doi.org/10.1002/chem.201700439.

[4] H. Huang, X. Wang, Recent progress on carbon-based support materials for electrocatalysts of direct methanol fuel cells, J. Mater. Chem. A 2 (2014) 6266–6291, https://doi.org/10.1039/c3ta14754a.

[5] J. Biener, M. Stadermann, M. Suss, M.A. Worsley, M.M. Biener, K.A. Rose, T. F. Baumann, Advanced carbon aerogels for energy applications, Energy Environ. Sci. 4 (2011) 656–667, https://doi.org/10.1039/c0ee00627k.

[6] C. Gao, X. Zhang, J. Zhan, B. Cai, Engineering of aerogel-based electrocatalysts for oxygen evolution reaction, Electrochem. Sci. Adv. 2 (2022) e2100113, https://doi.org/10.1002/elsa.202100113.

[7] X. Xu, H. Liang, F. Ming, Z. Qi, Y. Xie, Z. Wang, Prussian blue analogues derived penroseite (Ni,Co)Se_2 nanocages anchored on 3D graphene aerogel for efficient water splitting, ACS. Catal. 7 (2017) 6394–6399, https://doi.org/10.1021/acscatal.7b02079.

[8] Y. Yan, P. Wang, J. Lin, J. Cao, J. Qi, Modification strategies on transition metal-based electrocatalysts for efficient water splitting, J. Energy Chem. 58 (2021) 446–462, https://doi.org/10.1016/j.jechem.2020.10.010.

[9] Y. Wu, Y. Zhang, M.V. Nguyen, T.T.H. Chu, T.B.H. Nguyen, E.N. Dragoi, C. Xia, Latest insights on eco-friendly metal based-electrocatalyst for oxygen evolution reaction: challenges, and future perspectives, Mol. Catal. 534 (2023) 112818, https://doi.org/10.1016/j.mcat.2022.112818.

[10] Y. Sun, T. Zhang, C. Li, K. Xu, Y. Li, Compositional engineering of sulfides, phosphides, carbides, nitrides, oxides, and hydroxides for water splitting, J. Mater. Chem. A 8 (2020) 13415–13436, https://doi.org/10.1039/d0ta05038e.

[11] M. Zhang, X. Xuan, X. Yi, J. Sun, M. Wang, Y. Nie, J. Zhang, X. Sun, Carbon aerogels as electrocatalysts for sustainable energy applications: recent developments and prospects, Nanomaterials 12 (2022) 2721, https://doi.org/10.3390/nano12152721.

[12] N. Chandrasekaran, K.S. Adarsh, Pristine, transition metal and heteroatom-doped carbon aerogels for catalytic and electrocatalytic applications, Emerg. Carbon Mater. Catal. (2020) 235–253, https://doi.org/10.1016/B978-0-12-817561-3.00007-X.

[13] J.H. Lee, S.Y. Lee, S.J. Park, Highly porous carbon aerogels for high-performance supercapacitor electrodes, Nanomaterials 13 (2023) 817, https://doi.org/10.3390/nano13050817.

[14] A.V. Patil, S.A. Sawant, R.G. Sonkawade, R.S. Vhatkar, Green synthesized carbon aerogel for electric double layer capacitor, J. Energy Storage 72 (2023) 108533, https://doi.org/10.1016/j.est.2023.108533.

[15] B. Yao, H. Peng, H. Zhang, J. Kang, C. Zhu, G. Delgado, D. Byrne, S. Faulkner, M. Freyman, X. Lu, M.A. Worsley, J.Q. Lu, Y. Li, Printing porous carbon aerogels for low temperature supercapacitors, Nano Lett. 21 (2021) 3731–3737, https://doi.org/10.1021/acs.nanolett.0c04780.

[16] F.Y. Zeng, Z.Y. Sui, S. Liu, H.P. Liang, H.H. Zhan, B.H. Han, Nitrogen-doped carbon aerogels with high surface area for supercapacitors and gas adsorption, Mater. Today Commun. 16 (2018) 1–7, https://doi.org/10.1016/j.mtcomm.2018.03.015.

[17] Y. Cheng, H. Guo, X. Li, X. Wu, X. Xu, L. Zheng, R. Song, Rational design of ultrahigh loading metal single-atoms (Co, Ni, Mo) anchored on in-situ pre-crosslinked guar gum derived N-doped carbon aerogel for efficient overall water splitting, Chem. Eng. J. 410 (2021) 128359, https://doi.org/10.1016/j.cej.2020.128359.

[18] H. Li, X. Shu, P. Tong, J. Zhang, P. An, Z. Lv, H. Tian, J. Zhang, H. Xia, Fe–Ni alloy nanoclusters anchored on carbon aerogels as high-efficiency oxygen electrocatalysts in rechargeable Zn–air batteries, Small. 17 (2021) 2102002, https://doi.org/10.1002/smll.202102002.

[19] M. Samancı, E. Daş, A. Bayrakçeken Yurtcan, Carbon aerogel and their polypyrrole composites used as capacitive materials, Int. J. Energy Res. 45 (2021) 1729–1747, https://doi.org/10.1002/er.5841.

[20] D. Mladenović, M. Samancı, D.M.F. Santos, A. Bayrakçeken, B. Šljukić, Carbon aerogel and xerogel composites with polypyrrole as electrocatalysts for oxygen reduction reaction, Surf. Interfaces 60 (2025) 106071, https://doi.org/10.1016/J.SURFIN.2025.106071.

[21] T. Noor, L. Yaqoob, N. Iqbal, Recent advances in electrocatalysis of oxygen evolution reaction using noble-metal, transition-metal, and carbon-based materials, ChemElectroChem. 8 (2021) 447–483, https://doi.org/10.1002/celc.202001441.

[22] F. Rodríguez-Reinoso, The role of carbon materials in heterogeneous catalysis, Carbon. N. Y. 36 (1998) 159–175, https://doi.org/10.1016/S0008-6223(97)00173-5.

[23] M. Samancı, A. Bayrakçeken Yurtcan, Chemically and thermally reduced graphene oxide supported Pt catalysts prepared by supercritical deposition, Int. J. Hydrog. Energy 47 (2022) 19669–19689, https://doi.org/10.1016/j.ijhydene.2022.04.124.

[24] A. Hussain, M. Asim, M. Samanci, N. Kausar Janjua, A. Bayrakçeken, Oxygen evolution reaction activity of carbon aerogel supported Pd–Ni–Al catalysts synthesized by microwave irradiation method, Int. J. Hydrog. Energy 81 (2024) 93–109, https://doi.org/10.1016/J.IJHYDENE.2024.07.287.

[25] M. Samancı, M. Asim, A. Hussain, N.K. Janjua, A. Bayrakçeken, Microwave-assisted synthesis of Cu_xFe_{100-x}/Carbon aerogel (x = 0, 30, 50, 70) with enhanced electrocatalytic activity towards oxygen evolution reaction, J. Electroanal. Chem. 976 (2025) 118811, https://doi.org/10.1016/J.JELECHEM.2024.118811.

[26] M. Asim, A. Hussain, M. Samancı, N.K. Janjua, A. Bayrakçeken, Carbon aerogel supported Ni–Fe catalysts for superior oxygen evolution reaction activity, Carbon Lett. 34 (2024) 1779–1801, https://doi.org/10.1007/s42823-024-00730-4.

[27] A. Öztürk, N. Özçelik, A. Bayrakçeken Yurtcan, Platinum/graphene nanoplatelets/silicone rubber composites as polymer electrolyte membrane fuel cell catalysts, Mater. Chem. Phys. 260 (2021) 124110, https://doi.org/10.1016/j.matchemphys.2020.124110.

[28] A. Öztürk, A. Bayrakçeken Yurtcan, Preparation and characterization of melamine-led nitrogen-doped carbon blacks at different pyrolysis temperatures, J. Solid. State Chem. 296 (2021) 121972, https://doi.org/10.1016/j.jssc.2021.121972.

[29] Y.A. Kumar, K.D. Kumar, H.J. Kim, Reagents assisted $ZnCo_2O_4$ nanomaterial for supercapacitor application, Electrochim. Acta 330 (2020) 135261, https://doi.org/10.1016/J.ELECTACTA.2019.135261.

[30] H.J. Kim, B. Naresh, I.H. Cho, J.S. Bak, S.A. Hira, P.R. Sekhar Reddy, T.N. V. Krishna, K.Dasha Kumar, B.A. Mola, Y.A. Kumar, An advanced nano-sticks & flake-type architecture of manganese-cobalt oxide as an effective electrode material for supercapacitor applications, J. Energy Storage 40 (2021) 102702, https://doi.org/10.1016/J.EST.2021.102702.

[31] A.K. Yedluri, S. Sangaraju, S.H. Ahmed, Z. Kamran, U. Waqar, K.T.N. V, K.K. Dasha, M.O. Ihab, K. Hee-Je, Boosting the energy density of highly efficient flexible hybrid supercapacitors via selective integration of hierarchical nanostructured energy materials, Electrochim. Acta 364 (2020) 137318, https://doi.org/10.1016/J.ELECTACTA.2020.137318.

[32] G.I.N. Waterhouse, G.A. Bowmaker, J.B. Metson, Oxygen chemisorption on an electrolytic silver catalyst: a combined TPD and Raman spectroscopic study, Appl. Surf. Sci. 214 (2003) 36–51, https://doi.org/10.1016/S0169-4332(03)00350-7.

[33] S. van Dommele, A. Romero-Izquirdo, R. Brydson, K.P. de Jong, J.H. Bitter, Tuning nitrogen functionalities in catalytically grown nitrogen-containing carbon nanotubes, Carbon. N. Y. 46 (2008) 138–148, https://doi.org/10.1016/j.carbon.2007.10.034.

[34] M. Song, Y. Song, W. Sha, B. Xu, J. Guo, Y. Wu, Recent advances in non-precious transition metal/nitrogen-doped carbon for oxygen reduction electrocatalysts in PEMFCs, Catalysts. 10 (2020) 141, https://doi.org/10.3390/catal10010141.

[35] Y. Yamada, Y. Suzuki, H. Yasuda, S. Uchizawa, K. Hirose-Takai, Y. Sato, K. Suenaga, S. Sato, Functionalized graphene sheets coordinating metal cations, Carbon. N. Y. 75 (2014) 81–94, https://doi.org/10.1016/j.carbon.2014.03.036.

[36] M. Chen, G. Zhao, L.L. Shao, Z.Y. Yuan, Q.S. Jing, K.J. Huang, Z.Y. Huang, X. H. Zhao, G.D. Zou, Controlled synthesis of nickel encapsulated into nitrogen-doped carbon nanotubes with covalent bonded interfaces: the structural and electronic modulation strategy for an efficient electrocatalyst in dye-sensitized solar cells, Chem. Mat. 29 (2017) 9680–9694, https://doi.org/10.1021/acs.chemmater.7b03385.

[37] W. Jin, G. Maduraiveeran, Recent advances of porous transition metal-based nanomaterials for electrochemical energy conversion and storage applications, Mater. Today Energy 13 (2019) 64–84, https://doi.org/10.1016/j.mtener.2019.04.016.

[38] Y. Li, R. Tang, J. Liu, W. Zhou, J. Gao, H. Wu, Cobalt nanoparticles embedded in the N-doped carbon nanospheres as efficient oxygen catalysis for rechargeable flexible Zn-air batteries, J. Nanoparticle Res. 23 (2021) 131, https://doi.org/10.1007/s11051-021-05258-6.

[39] T. Yang, G. Han, Synthesis of a novel catalyst via pyrolyzing melamine with Fe precursor and its excellent electrocatalysis for oxygen reduction, Int. J. Electrochem. Sci. 7 (2012) 10884–10893, https://doi.org/10.1016/s1452-3981(23)16910-0.

[40] Q. Yan, J. Li, X. Zhang, E.B. Hassan, C. Wang, J. Zhang, Z. Cai, Catalytic graphitization of kraft lignin to graphene-based structures with four different transitional metals, J. Nanoparticle Res. 20 (2018) 223, https://doi.org/10.1007/s11051-018-4317-0.

[41] J.H. Ramirez, F.J. Maldonado-Hódar, A.F. Pérez-Cadenas, C. Moreno-Castilla, C. A. Costa, L.M. Madeira, Azo-dye Orange II degradation by heterogeneous Fenton-like reaction using carbon-Fe catalysts, Appl. Catal. B 75 (2007) 312–323, https://doi.org/10.1016/j.apcatb.2007.05.003.

[42] C. Zhang, M. Zhou, G. Ren, X. Yu, L. Ma, J. Yang, F. Yu, Heterogeneous electro-Fenton using modified iron-carbon as catalyst for 2,4-dichlorophenol degradation: influence factors, mechanism and degradation pathway, Water. Res. 70 (2015) 414–424, https://doi.org/10.1016/j.watres.2014.12.022.

[43] X. Li, D. Du, C. Wang, H. Wang, Z. Xu, In situ synthesis of hierarchical rose-like porous Fe@C with enhanced electromagnetic wave absorption, J. Mater Chem. C 6 (2018) 558–567, https://doi.org/10.1039/c7tc04897a.

[44] J. Mahmood, F. Li, C. Kim, H.J. Choi, O. Gwon, S.M. Jung, J.M. Seo, S.J. Cho, Y. W. Ju, H.Y. Jeong, G. Kim, J.B. Baek, Fe@C2N: a highly-efficient indirect-contact oxygen reduction catalyst, Nano Energy 44 (2018) 304–310, https://doi.org/10.1016/j.nanoen.2017.11.057.

[45] Y.M. Dai, C.Y. Lu, C.J. Chang, Catalytic activity of mesoporous Ni/CNT, Ni/SBA-15 and (Cu, Ca, Mg, Mn, Co)-Ni/SBA-15 catalysts for CO_2 reforming of CH_4, RSC. Adv. 6 (2016) 73887–73896, https://doi.org/10.1039/c6ra07635a.

[46] I. Gonzalez, J.C. De Jesus, E. Cañizales, B. Delgado, C. Urbina, Comparison of the surface state of Ni nanoparticles used for methane catalytic decomposition, J. Phys. Chem. C 116 (2012) 21577–21587, https://doi.org/10.1021/jp302372r.

[47] D. Xu, Y. Pan, M. Chen, Q. Pan, L. Zhu, M. Xue, D. Zhang, Q. Fang, S. Qiu, Synthesis and application of a MOF-derived Ni@C catalyst by the guidance from an: in situ

hot stage in TEM, RSC. Adv. 7 (2017) 26377–26383, https://doi.org/10.1039/c7ra03162a.
[48] S.A. Chernyak, A.S. Ivanov, S.V. Maksimov, K.I. Maslakov, O.Y. Isaikina, P. A. Chernavskii, R.V. Kazantsev, O.L. Eliseev, S.S. Savilov, Fischer-Tropsch synthesis over carbon-encapsulated cobalt and iron nanoparticles embedded in 3D-framework of carbon nanotubes, J. Catal. 389 (2020) 270–284, https://doi.org/10.1016/j.jcat.2020.06.011.
[49] Y. Wang, C. An, G. Liu, L. Li, Y. Wang, C. Chen, L. Jiao, H. Yuan, In situ synthesized one-dimensional porous Ni@C nanorods as catalysts for hydrogen storage properties of MgH_2, Nanoscale 6 (2014) 3223–3230, https://doi.org/10.1039/c3nr05607d.
[50] X. Sun, A. Gutierrez, M.J. Yacaman, X. Dong, S. Jin, Investigations on magnetic properties and structure for carbon encapsulated nanoparticles of Fe, Co, Ni, Mater. Sci. Eng. A 286 (2000) 157–160, https://doi.org/10.1016/S0921-5093(00)00628-6.
[51] S. Fang, Z. Cui, Y. Zhu, C. Wang, J. Bai, X. Zhang, Y. Xu, Q. Liu, L. Chen, Q. Zhang, L. Ma, In situ synthesis of biomass-derived Ni/C catalyst by self-reduction for the hydrogenation of levulinic acid to γ-valerolactone, J. Energy Chem. 37 (2019) 204–214, https://doi.org/10.1016/j.jechem.2019.03.021.
[52] X.J. Li, N. Luo, M.L. Bai, Synthesis and characterization of graphite-encapsulated metal (Fe,Co,Ni) nanoparticles by a detonation method, in: Materials Science Forum, 2011. https://doi.org/10.4028/www.scientific.net/MSF.673.161.
[53] A. Sharma, I. Saito, H. Nakagawa, K. Miura, Effect of carbonization temperature on the nickel crystallite size of a Ni/C catalyst for catalytic hydrothermal gasification of organic compounds, Fuel 86 (2007) 915–920, https://doi.org/10.1016/j.fuel.2006.11.001.
[54] L. Xing, J. Qiu, C. Liang, C. Wang, L. Mao, A new approach to high performance Co/C catalysts for selective hydrogenation of chloronitrobenzenes, J. Catal. 250 (2007) 369–372, https://doi.org/10.1016/j.jcat.2007.06.008.
[55] M. González-Castaño, J.C. Navarro de Miguel, J.H. Boelte, M.A. Centeno, O. Klepel, H. Arellano-García, Assessing the impact of textural properties in Ni–Fe catalysts for CO_2 methanation performance, Microporous Mesoporous Mater. 327 (2021) 111405, https://doi.org/10.1016/j.micromeso.2021.111405.
[56] A.A. El-Gendy, E.M.M. Ibrahim, V.O. Khavrus, Y. Krupskaya, S. Hampel, A. Leonhardt, B. Büchner, R. Klingeler, The synthesis of carbon coated Fe, Co and Ni nanoparticles and an examination of their magnetic properties, Carbon. N. Y. 47 (2009) 2821–2828, https://doi.org/10.1016/j.carbon.2009.06.025.
[57] M.R. Pallavolu, Y.A. Kumar, G. Mani, R.A. Alshgari, M. Ouladsmane, S.W. Joo, Facile fabrication of novel heterostructured tin disulfide (SnS_2)/tin sulfide (SnS)/N-CNO composite with improved energy storage capacity for high-performance supercapacitors, J. Electroanal. Chem. 899 (2021) 115695, https://doi.org/10.1016/j.jelechem.2021.115695.
[58] Y.A. Kumar, H.T. Das, P.R. Guddeti, R.R. Nallapureddy, M.R. Pallavolu, S. Alzahmi, I.M. Obaidat, Self-supported Co_3O_4@Mo-Co_3O_4 needle-like nanosheet heterostructured architectures of battery-type electrodes for high-performance asymmetric supercapacitors, Nanomaterials 12 (2022) 2330, https://doi.org/10.3390/nano12142330.
[59] B.A. Mola, M.R. Pallavolu, B.A. Al-Asbahi, Y. Noh, S.K. Jilcha, Y.A. Kumar, Design and construction of hierarchical $MnFe_2Ce_4$@$MnNiCe_4$ nanosheets on Ni foam as an advanced electrode for battery-type supercapacitor applications, J. Energy Storage 51 (2022) 104542, https://doi.org/10.1016/J.EST.2022.104542.
[60] S. Kim, S. Kato, T. Ishizaki, O.L. Li, J. Kang, Transition metal (Fe, Co, Ni) nanoparticles on selective Amino-N-doped carbon as high-performance oxygen reduction reaction electrocatalyst, Nanomaterials 9 (2019) 742, https://doi.org/10.3390/nano9050742.
[61] B. Hu, J.Y. Yuan, J.Y. Tian, M. Wang, X. Wang, L. He, Z. Zhang, Z.W. Wang, C. Sen Liu, Co/Fe-bimetallic organic framework-derived carbon-incorporated cobalt–ferric mixed metal phosphide as a highly efficient photocatalyst under visible light, J. Colloid. Interface Sci. 531 (2018) 148–159, https://doi.org/10.1016/j.jcis.2018.07.037.
[62] X. Chen, X. Wang, D. Fang, A review on C1s XPS-spectra for some kinds of carbon materials, Fuller. Nanotub. Carbon Nanostructures 28 (2020) 1048–1058, https://doi.org/10.1080/1536383X.2020.1794851.
[63] C. Deng, L. Xu, K. Hu, X. Chen, R. Gao, L. Zhang, L. Wang, C. Zhang, Research advances on nitrogen-doped carbon materials in CO_x hydrogenation, Atmos. (Basel) 14 (2023) 1510, https://doi.org/10.3390/atmos14101510.
[64] G. Azuara-Tuexi, E. Muñoz-Sandoval, R.A. Guirado-López, N 1s core-level binding energies in nitrogen-doped carbon nanotubes: a combined experimental and theoretical study, Phys. Chem. Chem. Phys. 25 (2023) 3718–3736, https://doi.org/10.1039/d2cp04701b.
[65] Y. Anil Kumar, S. Singh, D.K. Kulurumotlakatla, H.J. Kim, A $MoNiO_4$ flower-like electrode material for enhanced electrochemical properties via a facile chemical bath deposition method for supercapacitor applications, New J. Chem. 44 (2019) 522–529, https://doi.org/10.1039/C9NJ05529K.
[66] Y. Anil Kumar, K. Dasha Kumar, H.J. Kim, Facile preparation of a highly efficient $NiZn_2O_4$–NiO nanoflower composite grown on Ni foam as an advanced battery-type electrode material for high-performance electrochemical supercapacitors, Dalton. Trans. 49 (2020) 3622–3629, https://doi.org/10.1039/D0DT00268B.
[67] C.C.L. McCrory, S. Jung, J.C. Peters, T.F. Jaramillo, Benchmarking heterogeneous electrocatalysts for the oxygen evolution reaction, J. Am. Chem. Soc. 135 (2013) 16977–16987, https://doi.org/10.1021/ja407115p.
[68] Y. Su, Y. Zhu, H. Jiang, J. Shen, X. Yang, W. Zou, J. Chen, C. Li, Cobalt nanoparticles embedded in N-doped carbon as an efficient bifunctional electrocatalyst for oxygen reduction and evolution reactions, Nanoscale 6 (2014) 15080–15089, https://doi.org/10.1039/c4nr04357j.
[69] A. Zabielaite, A. Balciunaite, D. Upskuviene, D. Simkunaite, R. Levinas, G. Niaura, J. Vaiciuniene, V. Jasulaitiene, L. Tamasauskaite-Tamasiunaite, E. Norkus, Investigation of hydrogen and oxygen evolution on cobalt-nanoparticles-supported graphitic carbon nitride, Mater. (Basel) 16 (2023) 5923, https://doi.org/10.3390/ma16175923.
[70] X. Yu, Z. Pan, Z. Zhao, Y. Zhou, C. Pei, Y. Ma, H.S. Park, M. Wang, Boosting the oxygen evolution reaction by controllably constructing $FeNi_3$/C nanorods, Nanomaterials 12 (2022) 2525, https://doi.org/10.3390/nano12152525.
[71] J.R. Swierk, S. Klaus, L. Trotochaud, A.T. Bell, T.D. Tilley, Electrochemical study of the energetics of the oxygen evolution reaction at nickel iron (oxy)hydroxide catalysts, J. Phys. Chem. C 119 (2015) 19022–19029, https://doi.org/10.1021/acs.jpcc.5b05861.
[72] H.C. Chien, W.Y. Cheng, Y.H. Wang, S.Y. Lu, Ultrahigh specific capacitances for supercapacitors achieved by nickel cobaltite/carbon aerogel composites, Adv. Funct. Mater. 22 (2012), https://doi.org/10.1002/adfm.201201176.
[73] K.I. Nargatti, A.R. Subhedar, S.S. Ahankari, A.N. Grace, A. Dufresne, Nanocellulose-based aerogel electrodes for supercapacitors: a review, Carbohydr. Polym. 297 (2022) 120039, https://doi.org/10.1016/j.carbpol.2022.120039.
[74] J. Rupar, D. Bajuk-Bogdanović, M. Milojević-Rakić, J. Krstić, K. Upadhyay, N. Gavrilov, A.Janošević Ležaić, Tailored porosity development in carbons via Zn^{2+} monodispersion: fitting supercapacitors, Microporous Mesoporous Mater. 335 (2022) 111790, https://doi.org/10.1016/j.micromeso.2022.111790.
[75] D.K. Kulurumotlakatla, A.K. Yedluri, H.-J. Kim, Hierarchical $NiCo_2S_4$ nanostructure as highly efficient electrode material for high-performance supercapacitor applications, J. Energy Storage 31 (2020) 101619, https://doi.org/10.1016/j.est.2020.101619.
[76] M. Moniruzzaman, Y.A. Kumar, M.R. Pallavolu, H.M. Arbi, S. Alzahmi, I. M. Obaidat, Two-dimensional core-shell structure of cobalt-doped@MnO_2 nanosheets grown on nickel foam as a binder-free battery-type electrode for supercapacitor application, Nanomater 12 (2022) 3187, https://doi.org/10.3390/nano12183187.
[77] Y. Lv, C. Qi, Y. Bai, L. Li, S. Chen, Z. He, P. Wu, S. Zhang, One-step self-assembled biomass carbon aerogel/carbon nanotube/cellulose nanofiber composite for supercapacitor flexible electrode, Diam. Relat. Mater. 149 (2020) 111530, https://doi.org/10.1016/j.diamond.2024.111530.
[78] B. Thomas, G. George, A. Landström, I. Concina, S. Geng, A. Vomiero, M. Sain, K. Oksman, Electrochemical properties of biobased carbon aerogels decorated with graphene dots synthesized from biochar, ACS. Appl. Electron. Mater. 3 (2023) 4699, https://doi.org/10.1021/acsaelm.1c00487.
[79] X. Tang, S. Xia, Q. Luo, J. Liu, H. Gong, Y. Deng, X. Chen, J. Shao, Hierarchically porous graphene aerogels with abundant oxygenated groups for high-energy-density supercapacitors, Energ Fuels 36 (2022), https://doi.org/10.1021/acs.energyfuels.2c02723.
[80] Z. Zhai, B. Ren, Y. Xu, S. Wang, L. Zhang, Z. Liu, Nitrogen self-doped carbon aerogels from chitin for supercapacitors, J. Power. Sources. 481 (2021) 228976, https://doi.org/10.1016/j.jpowsour.2020.228976.
[81] C.Y. Lee, H.M. Tsai, H.J. Chuang, S.Y. Li, P. Lin, T.Y. Tseng, Characteristics and electrochemical performance of supercapacitors with manganese oxide-carbon nanotube nanocomposite electrodes, J. Electrochem. Soc. 152 (2005) A716, https://doi.org/10.1149/1.1870793.
[82] N. Nagarajan, M. Cheong, I. Zhitomirsky, Electrochemical capacitance of MnO_x films, Mater. Chem. Phys. 103 (2007) 47–53, https://doi.org/10.1016/j.matchemphys.2007.01.005.
[83] K.D. Kumar, T. Ramachandran, Y.A. Kumar, A.A.A. Mohammed, M.C. Kang, Hierarchically fabricated nano flakes-rod-like CoMoO–S supported Ni-foam for high-performance supercapacitor electrode material, J. Phys. Chem. Solids. 185 (2024) 111735, https://doi.org/10.1016/j.jpcs.2023.111735.
[84] K.D. Kumar, Y.A. Kumar, T. Ramachandran, A.A. Al-Kahtani, M.C. Kang, Cactus-Like Ni-Co/$CoMn_2O_4$ composites on Ni foam: unveiling the potential for advanced electrochemical materials for pseudocapacitors, Mater. Sci. Engin: B 296 (2023) 116715, https://doi.org/10.1016/j.mseb.2023.116715.